



HAL
open science

Internal shear layers in librating spherical shells: the case of attractors

Jiyang He, Benjamin Favier, Michel Rieutord, Stéphane Le Dizès

► **To cite this version:**

Jiyang He, Benjamin Favier, Michel Rieutord, Stéphane Le Dizès. Internal shear layers in librating spherical shells: the case of attractors. *Journal of Fluid Mechanics*, 2023, 974, 10.1017/jfm.2023.761 . hal-04286209

HAL Id: hal-04286209

<https://hal.science/hal-04286209>

Submitted on 15 Nov 2023

HAL is a multi-disciplinary open access archive for the deposit and dissemination of scientific research documents, whether they are published or not. The documents may come from teaching and research institutions in France or abroad, or from public or private research centers.

L'archive ouverte pluridisciplinaire **HAL**, est destinée au dépôt et à la diffusion de documents scientifiques de niveau recherche, publiés ou non, émanant des établissements d'enseignement et de recherche français ou étrangers, des laboratoires publics ou privés.

Banner appropriate to article type will appear here in typeset article

1 **Internal shear layers in librating spherical shells:** 2 **the case of attractors**

3 **Jiyang He¹ †, Benjamin Favier¹, Michel Rieutord² and Stéphane Le Dizès¹**

4 ¹Aix Marseille Univ, CNRS, Centrale Marseille, IRPHE, F-13384 Marseille, France

5 ²IRAP, Université de Toulouse, CNRS, UPS, CNES, 14 avenue Édouard Belin, F-31400 Toulouse, France

6 (Received xx; revised xx; accepted xx)

7 Following our previous work on periodic ray paths (He *et al.* 2022), we study asymptotically
8 and numerically the structure of internal shear layers for very small Ekman numbers in a three-
9 dimensional (3D) spherical shell and in a two-dimensional (2D) cylindrical annulus when
10 the rays converge towards an attractor. We first show that the asymptotic solution obtained
11 by propagating the self-similar solution generated at the critical latitude on the librating
12 inner core describes the main features of the numerical solution. The internal shear layer
13 structure and the scaling for its width and velocity amplitude in $E^{1/3}$ and $E^{1/12}$ respectively
14 are recovered. The amplitude of the asymptotic solution is shown to decrease to $E^{1/6}$ when
15 it reaches the attractor, as is also observed numerically. However, some discrepancies are
16 observed close to the particular attractors along which the phase of the wave beam remains
17 constant. Another asymptotic solution close to those attractors is then constructed using the
18 model of Ogilvie (2005). The solution obtained for the velocity has an $O(E^{1/6})$ amplitude,
19 but a different self-similar structure than the critical-latitude solution. It also depends on the
20 Ekman pumping at the contact points of the attractor with the boundaries. We demonstrate
21 that it reproduces correctly the numerical solution. Surprisingly, the numerical solution close
22 to an attractor with phase shift (that is an attractor touching the axis in 3D or in 2D with a
23 symmetric forcing) is also found to be $O(E^{1/6})$ but its amplitude is much weaker. However,
24 its asymptotic structure remains a mystery.

25 **1. Introduction**

26 In rotating flows, inertial waves with a frequency smaller than twice the rotation rate propagate
27 at a fixed angle with respect to the rotation axis (Greenspan 1968). The frequency and the
28 angle are preserved when inertial waves reflect on a boundary. However, an inertial wave
29 beam may contract or expand as it reflects. This linear contraction effect is responsible for
30 inviscid singularities in the inertial wave field (Ogilvie 2020; Rieutord *et al.* 2001).

31 There are two types of inviscid singularities concerned in the present work. One is at the
32 critical latitude of a sphere where the rays are tangent to the boundary and where Ekman
33 pumping blows up (Roberts & Stewartson 1963). This singularity propagates within the fluid
34 along the tangent critical line at the critical latitude (Kerswell 1995). When regularised by
35 viscosity, it forms concentrated internal shear layers around the critical line. The viscous self-
36 similar solution of Moore & Saffman (1969) and Thomas & Stevenson (1972) is expected to

† Email address for correspondence: jiyanghe123@gmail.com

37 describe the viscous structure of these thin layers for small Ekman numbers. For a librating
38 spheroid, Le Dizès & Le Bars (2017) derived the singularity strength and the amplitude of
39 the self-similar solution by asymptotically matching the shear layer solution with the Ekman
40 layer solution. The self-similar solution was found to be in agreement with direct numerical
41 simulation. The same self-similar solution (with the singularity strength and the amplitudes
42 derived in an open domain) was also used to describe the solution on a periodic orbit in a
43 spherical shell geometry (He *et al.* 2022, hereafter HFRL22). In that case, the solution was
44 obtained by considering its propagation along the periodic orbit for an infinite number of
45 cycles. It was found to agree very well with the numerical solutions obtained for low Ekman
46 numbers. In particular both the internal shear layer structure and its amplitude scaling in
47 $E^{1/12}$ were recovered by the numerical results using Ekman numbers as low as 10^{-10} .

48 The singularity obtained from the critical latitude on the outer sphere gives rise to different
49 internal shear layers. These layers are weaker, thicker and do not possess a self-similar
50 structure (Kerswell 1995; Lin & Noir 2021). Kida (2011) obtained their asymptotic structure
51 for a precessing sphere.

52 Besides libration and precession which drive the flows through viscosity, non-viscous
53 forcing associated with translating or deforming bodies have also been analysed. Many
54 studies have been performed in the context of stratified fluids for applications to tidal flows.
55 Analytic results were obtained for the cylinder and the sphere in an unbounded geometry
56 (Hurley 1997; Hurley & Keady 1997; Voisin 2003) and validated experimentally in both
57 2D (Sutherland & Linden 2002; Zhang *et al.* 2007) and 3D (Flynn *et al.* 2003; Voisin *et al.*
58 2011; Ghaemsaidi & Peacock 2013). Hurley & Keady (1997) and Voisin (2003) also showed
59 that, in the far-field, the solution takes the self-similar form predicted by Moore & Saffman
60 (1969). The singularity strength however varies with respect to the nature of the forcing.
61 Machicoane *et al.* (2015) discussed this effect for pulsating and oscillating spheres.

62 The other inviscid singularity is the attractor in a closed container onto which inertial
63 waves tend to focus (Rieutord & Valdettaro 1997). The presence of such singularities is
64 related to the hyperbolic character of the Poincaré equation describing the wave structure:
65 it leads to an ill-posed Cauchy problem except for a few geometries such as the cylinder
66 or the ellipsoid (Rieutord *et al.* 2000). Contrary to the singularity attached to the boundary
67 at the critical latitude, the attractor is a limit cycle which is not directly dependent on
68 the nature of the forcing. Attractors also generate intense internal shear layers, as first
69 observed in a trapezoidal tank for a stably stratified fluid (Maas *et al.* 1997). The asymptotic
70 structure of these layers was analysed in a forced regime in 2D by Ogilvie (2005) (hereafter
71 O05). Under a few technical hypotheses, he was able to derive the functional equation
72 describing the inviscid streamfunction and to provide the viscous asymptotic expression of
73 the streamfunction close to the attractor. In particular, O05 showed that, for his quadrilateral
74 geometry possessing a unique attractor, the main contribution to the solution is associated
75 with the logarithmic singularity of the inviscid streamfunction. We shall use and adapt his
76 results to our geometry. His results were confirmed by a numerical study of an inclined
77 rotating square in Jouve & Ogilvie (2014).

78 In a spherical shell, there may exist both critical-latitude and attractor singularities at the
79 same time. In HFRL22, we have considered a case where no attractor was present. We have
80 assumed that the fluid was forced by librating the inner core at a frequency such that inertial
81 waves propagated in a direction oriented at 45° with respect to the rotation axis. All the
82 ray trajectories were periodic in that case, and the (critical) path issued from the critical
83 latitude on the inner core was just a rectangle in the upper left meridional cut of the shell. For
84 other frequencies, the rays issued from the critical latitude are expected to perform a more
85 complex pattern and possibly converge to an attractor (Tilgner 1999; Ogilvie & Lin 2004;
86 Ogilvie 2009). It is this situation we want to address in the present work. We consider the

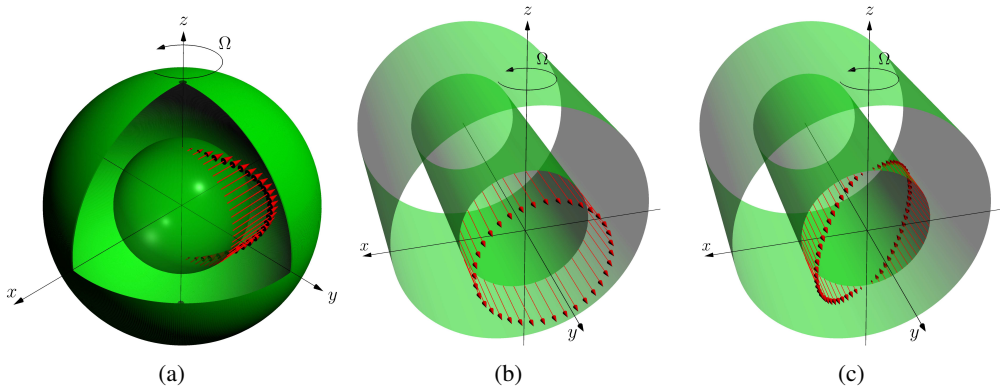


Figure 1: Configurations: (a) a 3D spherical shell subject to the longitudinal libration on the inner core; (b) a 2D cylindrical annulus subject to the symmetric forcing on the inner core; (c) a 2D cylindrical annulus subject to the antisymmetric forcing on the inner core. The red arrows show the magnitudes and the directions of the forcings at one instant.

87 same framework as in HFRL22, where local asymptotic solutions propagated in the volume
 88 are compared with global numerical results, but for a frequency for which an attractor is now
 89 present.

90 The paper is organised as follows. The framework is introduced in section § 2. In
 91 § 2.1, we describe the 3D and 2D configurations that we have considered, and provide
 92 the governing equations. In § 2.2, the numerical method used to integrate the equations for
 93 each configuration is explained. In section § 3, we first analyse the wave beams emitted
 94 from the critical latitude on the inner core. The asymptotic solution built by propagating
 95 the self-similar solution is compared to the numerical solution. Discrepancies are observed
 96 close to the attractors for some of the cases. In section § 4, we then focus on the solution
 97 close to the attractors. We construct an asymptotic solution based on the theory of O05 for
 98 an attractor without phase shift in §4.1, and provide a numerical validation in §4.2. A brief
 99 conclusion is finally provided in section § 5.

100 2. Framework

101

2.1. Configurations

102 In this paper, we consider the flow of an incompressible fluid of constant kinematic viscosity
 103 ν^* rotating around the axis e_z with a uniform rotation rate Ω^* . We consider two different
 104 configurations. The first one is the axisymmetric flow filling a three-dimensional (3D)
 105 spherical shell, as in HFRL22. The other configuration is the two-dimensional (2D) flow, but
 106 with three velocity components, between two co-axial cylinders whose axis is horizontal,
 107 as in Rieutord *et al.* (2002) and Rieutord & Valdettaro (2010). In the following, geometries,
 108 governing equations and forcings are described separately for the two configurations.

109 2.1.1. 3D configuration

110 The geometry of the 3D spherical shell is shown in figure 1a, whose meridional plane can
 111 be found in figure 2 of HFRL22. The radii of the outer and inner spheres are ρ^* and $\eta\rho^*$
 112 (with $0 < \eta < 1$ the aspect ratio), respectively. Lengths are non-dimensionalised by the
 113 outer radius ρ^* such that the inner and outer dimensionless radii are η and 1 respectively.
 114 Time is non-dimensionalised by the angular period $1/\Omega^*$. The imposed harmonic forcing is
 115 the libration of one of the two boundaries, with the amplitude $\varepsilon = \varepsilon^*/\Omega^*$ ($\varepsilon \ll 1$) and the

116 frequency $\omega = \omega^*/\Omega^*$. The Ekman number is defined as

$$117 \quad E = \frac{\nu^*}{\Omega^* \rho^{*2}}, \quad (2.1)$$

118 with ν^* being the kinematic viscosity.

119 As in HFRL22, we care about the linear harmonic response when the Ekman number is
120 extremely small. We look for solutions that are harmonic in time

$$121 \quad \varepsilon(\mathbf{v}, p)e^{-i\omega t} + c.c. \quad (2.2)$$

with *c.c.* denoting complex conjugation. The velocity \mathbf{v} and pressure p satisfy the linearised incompressible Navier-Stokes equations in the rotating frame

$$-i\omega\mathbf{v} + 2\mathbf{e}_z \times \mathbf{v} = -\nabla p + E\nabla^2\mathbf{v}, \quad (2.3a)$$

$$\nabla \cdot \mathbf{v} = 0. \quad (2.3b)$$

In terms of the velocity components and pressure, the governing equations in the cylindrical coordinate system (r, z, ϕ) become

$$-i\omega v_r - 2v_\phi + \frac{\partial p}{\partial r} - E\left(\nabla^2 - \frac{1}{r^2}\right)v_r = 0, \quad (2.4a)$$

$$-i\omega v_z + \frac{\partial p}{\partial z} - E\nabla^2 v_z = 0, \quad (2.4b)$$

$$-i\omega v_\phi + 2v_r - E\left(\nabla^2 - \frac{1}{r^2}\right)v_\phi = 0, \quad (2.4c)$$

$$\frac{\partial v_r}{\partial r} + \frac{v_r}{r} + \frac{\partial v_z}{\partial z} = 0, \quad (2.4d)$$

122 with the Laplacian operator

$$123 \quad \nabla^2 = \frac{\partial^2}{\partial r^2} + \frac{1}{r} \frac{\partial}{\partial r} + \frac{\partial^2}{\partial z^2}. \quad (2.5)$$

124 The fluid is subject to no-slip boundary conditions on all boundaries. One of the two
125 boundaries is subject to the longitudinal libration as shown by the red arrows in figure
126 **1a**, which corresponds to the oscillating solid body rotation of the boundary according to

$$127 \quad \mathbf{v}(\rho) = r\mathbf{e}_\phi \quad \text{at} \quad \rho = \eta \quad \text{or} \quad 1, \quad (2.6)$$

128 while the other boundary is not moving

$$129 \quad \mathbf{v}(\rho) = \mathbf{0} \quad \text{at} \quad \rho = 1 \quad \text{or} \quad \eta. \quad (2.7)$$

130 r is the distance to the rotation axis of the cylindrical coordinate system (r, z, ϕ) , while
131 $\rho = \sqrt{r^2 + z^2}$ is distance to the centre in the spherical coordinate system.

132 2.1.2. 2D configuration

We also consider a 2D simplification of the 3D axisymmetric configuration discussed above. The geometry can be viewed as a slender cored torus with the principal radius tending to infinity (Rieutord *et al.* 2002; Rieutord & Valdettaro 2010), which is effectively equivalent to two co-axial cylinders whose principal axis is horizontal, as shown in figures **1b** and **1c**. The flow between the two cylinders satisfies the similar governing equations as (2.3), while the curvature terms in the differential operators, such as $1/r$, $1/r\partial/\partial r$ and $1/r^2$, are omitted.

Explicitly, in terms of the velocity components and pressure, the governing equations are

$$-i\omega v_x - 2v_y + \frac{\partial p}{\partial x} - E\nabla^2 v_x = 0, \quad (2.8a)$$

$$-i\omega v_z + \frac{\partial p}{\partial z} - E\nabla^2 v_z = 0, \quad (2.8b)$$

$$-i\omega v_y + 2v_x - E\nabla^2 v_y = 0, \quad (2.8c)$$

$$\frac{\partial v_x}{\partial x} + \frac{\partial v_z}{\partial z} = 0, \quad (2.8d)$$

133 with the Laplacian operator

$$134 \quad \nabla^2 = \partial^2/\partial x^2 + \partial^2/\partial z^2. \quad (2.9)$$

135 We use (x, y, z) to denote the Cartesian coordinates, where Ox and Oz are the horizontal
136 and vertical axes respectively and Oy is along the direction perpendicular to the Oxz plane,
137 as shown in figures **1b** and **1c**. Note that although we use the same symbol for the Laplacian
138 operators in 2D and 3D, there is no ambiguity since the 2D and 3D operators are independently
139 used in the corresponding dimensions.

140 Similar to libration in the 3D configuration, the imposed forcing should be on the boundary.
141 We also require that it drives the fluid in the bulk through viscous coupling only. The direction
142 of the forcing is thus aligned with that of \mathbf{e}_y perpendicular to the Oxz plane. We consider
143 two options for the amplitude of the forcing. One option is that the amplitude is a constant,
144 which is

$$145 \quad \mathbf{v}(\varrho) = \mathbf{e}_y \quad \text{at} \quad \varrho = \eta \quad \text{or} \quad 1, \quad (2.10)$$

146 where $\varrho = \sqrt{x^2 + z^2}$. The cylinder subject to this forcing is expected to oscillate uniformly
147 along the direction \mathbf{e}_y , as shown by the red arrows in figure **1b**. The other option is that the
148 amplitude of the forcing depends linearly on the horizontal coordinate x , which is

$$149 \quad \mathbf{v}(\varrho) = x\mathbf{e}_y \quad \text{at} \quad \varrho = \eta \quad \text{or} \quad 1. \quad (2.11)$$

150 The cylinder subject to this forcing oscillates non-uniformly inducing shear at the inner
151 boundary, as shown by the red arrows in figure **1c**. While unrealistic from an experimental
152 point of view, it is a mathematically well-posed boundary condition and provides another
153 symmetry as discussed later. While the formula for the 2D antisymmetric forcing (2.11) is
154 similar to the 3D libration case (2.6), they differ in that the horizontal coordinate x in the 2D
155 configuration can be negative.

156 Both forcings are symmetric about the horizontal axis Ox . However, the former forcing
157 (2.10) is symmetric about the vertical axis Oz , while the latter (2.11) is antisymmetric about
158 Oz ; see the red arrows in figures **1b** and **1c** respectively. These two forcings are thus referred
159 to as symmetric and antisymmetric forcings respectively, according to their symmetries about
160 the Oz axis. They are also imposed on one of the two boundaries, while the other boundary
161 condition is no-slip.

162 In summary, we consider three different forcings, which are referred to as the 3D libration
163 (2.6), 2D symmetric (2.10) and 2D antisymmetric (2.11) forcings. The first one is defined
164 in the 3D spherical shell, while the latter two correspond to the 2D cylindrical annulus.
165 Note that we restrict our study to purely axisymmetric situations, so that we ignore zonally
166 propagating waves which require azimuthal inhomogeneities as discussed by Rabitti & Maas
167 (2013).

2.2. Numerical methods

168

169 The governing equations (2.3) are solved numerically by spectral methods for both the 3D
170 and 2D configurations. We actually solve the vorticity equation, which is the curl of the
171 momentum equations (2.3(a))

172

$$-i\omega\nabla \times \mathbf{v} + 2\nabla \times (\mathbf{e}_z \times \mathbf{v}) = E\nabla \times (\nabla^2 \mathbf{v}). \quad (2.12)$$

173

In the 2D configuration, the curl is only taken in the Oxz plane. The numerical methods are
174 different for the two configurations. Therefore, they are presented separately.

175

2.2.1. 3D configuration

176

177

178

179

In the 3D configuration, the numerical method is similar to that in our former work (HFRL22).
The governing equations are solved in the spherical coordinates (ρ, θ, ϕ) with ρ the distance
to the centre, θ the colatitude and ϕ the azimuthal angle. The velocity is expanded onto the
vector spherical harmonics in the angular directions

180

$$\mathbf{v} = \sum_{l=0}^{+\infty} \sum_{m=-l}^{+l} u_l^m(\rho) \mathbf{R}_l^m + v_l^m(\rho) \mathbf{S}_l^m + w_l^m(\rho) \mathbf{T}_l^m, \quad (2.13)$$

181 with

182

$$\mathbf{R}_l^m = Y_l^m(\theta, \phi) \mathbf{e}_\rho, \quad \mathbf{S}_l^m = \nabla Y_l^m, \quad \mathbf{T}_l^m = \nabla \times \mathbf{R}_l^m. \quad (2.14)$$

The gradients are taken on the unit sphere. The vorticity equation (2.12) is projected onto
the basis. u^l and w^l satisfy a set of ordinary differential equations

$$E\Delta_l w^l + i\omega w^l = -2A_l \rho^{l-1} \frac{\partial}{\partial \rho} \left(\frac{u^{l-1}}{\rho^{l-2}} \right) - 2A_{l+1} \rho^{-l-2} \frac{\partial}{\partial \rho} \left(\rho^{l+3} u^{l+1} \right), \quad (2.15a)$$

$$E\Delta_l \Delta_l (\rho u^l) + i\omega \Delta_l (\rho u^l) = 2B_l \rho^{l-1} \frac{\partial}{\partial \rho} \left(\frac{w^{l-1}}{\rho^{l-1}} \right) + 2B_{l+1} \rho^{-l-2} \frac{\partial}{\partial \rho} \left(\rho^{l+2} w^{l+1} \right), \quad (2.15b)$$

183 with

184

$$A_l = \frac{1}{l^2 \sqrt{4l^2 - 1}}, \quad B_l = l^2(l^2 - 1)A_l, \quad \Delta_l = \frac{d^2}{d\rho^2} + \frac{2}{\rho} \frac{d}{d\rho} - \frac{l(l+1)}{\rho^2}, \quad (2.16)$$

185

186

(e.g. Rieutord 1991). Axisymmetry ($m = 0$) is employed. v^l is related to u^l through the
continuity equation

187

$$v^l = \frac{1}{\rho l(l+1)} \frac{d\rho^2 u^l}{d\rho}. \quad (2.17)$$

188

One of the two boundaries is subject to the no-slip boundary condition

189

$$w^l = u^l = \frac{du^l}{d\rho} = 0 \quad \text{at} \quad \rho = 1 \quad \text{or} \quad \eta. \quad (2.18)$$

190

191

The other boundary is subject to the libration (2.6), whose projection onto the spherical
harmonics yields the inhomogeneous boundary condition

192

$$w^l = 2\sqrt{\frac{\pi}{3}} \rho \delta_{1,l}, \quad u^l = \frac{du^l}{d\rho} = 0 \quad \text{at} \quad \rho = \eta \quad \text{or} \quad 1. \quad (2.19)$$

193

194

$\delta_{1,l}$ is the Kronecker symbol. Note that the libration is imposed on the spherical harmonic
degree $l = 1$.

195

The equations (2.15-2.19) are truncated to the spherical harmonic degree L . The derivatives

196 to the radial coordinate ρ are replaced by the Chebyshev differentiation matrices at $N + 1$
 197 collocation points of the Gauss-Lobatto grid. Then a block tridiagonal system is obtained as

$$198 \quad \begin{bmatrix} \mathbf{D}_1 & \mathbf{C}_1 & & & & \\ \mathbf{B}_1 & \mathbf{D}_2 & \mathbf{C}_2 & & & \\ & & \ddots & \ddots & \ddots & \\ & & & \mathbf{B}_{L-1} & \mathbf{D}_{L-1} & \mathbf{C}_{L-1} \\ & & & & \mathbf{B}_L & \mathbf{D}_L \end{bmatrix} \begin{bmatrix} \mathbf{w}^1 \\ \rho \mathbf{u}^2 \\ \vdots \\ \mathbf{w}^{L-1} \\ \rho \mathbf{u}^L \end{bmatrix} = \begin{bmatrix} \mathbf{b}_1 \\ \mathbf{b}_2 \\ \vdots \\ \mathbf{b}_{L-1} \\ \mathbf{b}_L \end{bmatrix}. \quad (2.20)$$

199 The blocks within the coefficient matrix and the vectors are $(N + 1) \times (N + 1)$ and $(N + 1) \times 1$,
 200 respectively. The order of the coefficient matrix is $(N + 1)L$ and the number of non-zero
 201 elements is $(N + 1)^2(3L - 2)$. This block tridiagonal system is usually solved by a LU solver
 202 (Rieutord & Valdetaro 1997), by which the coefficient matrix is stored in the banded matrix
 203 format and the number of elements in memory is $(N + 1)^2(4L - 4) - (N + 1)(L - 2)$. On the
 204 other hand, the block tridiagonal system can be solved by the block version of the standard
 205 tridiagonal algorithm (also called Thomas algorithm), which is the Gaussian elimination
 206 on a block tridiagonal system. This method has been utilised by Ogilvie & Lin (2004). The
 207 algorithm can be found in Engeln-Meullges & Uhlig (1996) (p.121). The elimination is
 208 advanced forward from the lowest spherical harmonic degree to the highest and the block
 209 tridiagonal matrix is reduced to a block upper bidiagonal one, then the solution is obtained
 210 by backward substitution. During the forward elimination, the updated diagonal block \mathbf{D}_l is
 211 factorized by the LU solver. A partial pivoting of the block is employed in order to improve
 212 the numerical stability.

213 The three blocks \mathbf{B}_l , \mathbf{D}_l and \mathbf{C}_l and the inhomogeneous term \mathbf{b}_l at the spherical harmonic
 214 degree l are only needed when they take part in the forward elimination. Hence, the storage of
 215 the whole coefficient matrix is unnecessary. However, all the updated super diagonal blocks
 216 \mathbf{C}_l should be reserved in memory for the backward substitution. Their size is $(N + 1)^2(L - 1)$,
 217 which is almost one third of that of non-zero elements in the original coefficient matrix and
 218 one fourth of that in the banded matrix format required by the global LU solver. Therefore,
 219 the memory usage of the block tridiagonal algorithm is much less than that of the global LU
 220 solver, especially when L and N are very large, as required for very low Ekman numbers.
 221 We develop a code based on the block tridiagonal algorithm using the efficient dynamic
 222 programming language Julia (Bezanson *et al.* 2017). For now, we can reach $E = 10^{-11}$ by
 223 using 8000 spherical harmonics and 2500 Chebyshev polynomials using double precision
 224 floating-point format. The memory footprint is around 750GB.

225 2.2.2. 2D configuration

226 In the 2D configuration, we take the numerical method similar to that adopted by
 227 Rieutord *et al.* (2002) and Rieutord & Valdetaro (2010). The vorticity equation (2.12) is
 228 solved in the polar coordinates (ϱ, ϑ) with ϱ the distance to the centre and ϑ the angle
 229 measured from the horizontal axis Ox . In terms of the streamfunction ψ and the associated
 230 variable χ

$$231 \quad v_\varrho = -\frac{1}{\varrho} \frac{\partial \psi}{\partial \vartheta}, \quad v_\vartheta = \frac{\partial \psi}{\partial \varrho}, \quad v_y = \chi, \quad (2.21)$$

the vorticity equation is recast to

$$-i\omega \nabla^2 \psi + 2(\sin \vartheta \frac{\partial \chi}{\partial \varrho} + \frac{\cos \vartheta}{\varrho} \frac{\partial \chi}{\partial \vartheta}) - E \nabla^4 \psi = 0, \quad (2.22a)$$

$$-i\omega \chi - 2(\sin \vartheta \frac{\partial \psi}{\partial \varrho} + \frac{\cos \vartheta}{\varrho} \frac{\partial \psi}{\partial \vartheta}) - E \nabla^2 \chi = 0, \quad (2.22b)$$

232 with the operator

$$233 \quad \nabla^2 = \frac{\partial^2}{\partial \varrho^2} + \frac{1}{\varrho} \frac{\partial}{\partial \varrho} + \frac{1}{\varrho^2} \frac{\partial^2}{\partial \theta^2}. \quad (2.23)$$

The streamfunction ψ and the associated variable χ are expanded by Fourier series in the angular direction as

$$\psi = \sum_{l=-\infty}^{+\infty} \psi_l(\varrho) e^{il\theta}, \quad \chi = -i \sum_{l=-\infty}^{+\infty} \chi_l(\varrho) e^{il\theta}. \quad (2.24a, b)$$

The projection of the governing equations (2.22) onto this basis is

$$i\omega \nabla_l^2 \psi_l + (\chi'_{l-1} - \chi'_{l+1}) - \frac{1}{\varrho} [(l-1)\chi_{l-1} + (l+1)\chi_{l+1}] + E \nabla_l^4 \psi_l = 0, \quad (2.25a)$$

$$i\omega \chi_l + (\psi'_{l-1} - \psi'_{l+1}) - \frac{1}{\varrho} [(l-1)\psi_{l-1} + (l+1)\psi_{l+1}] + E \nabla_l^2 \chi_l = 0, \quad (2.25b)$$

234 with

$$235 \quad \nabla_l^2 = \frac{d^2}{d\varrho^2} + \frac{1}{\varrho} \frac{d}{d\varrho} - \frac{l^2}{\varrho^2}. \quad (2.26)$$

236 The unforced boundary is subject to the no-slip boundary condition

$$237 \quad \psi_l = \frac{d\psi_l}{d\varrho} = \chi_l = 0 \quad \text{at} \quad \varrho = 1 \quad \text{or} \quad \eta. \quad (2.27)$$

238 The other boundary is subject to the viscous boundary forcings (2.10, 2.11). Both forcings
239 are symmetric about the horizontal axis Ox , which leads to

$$240 \quad \psi_{-l} = -\psi_l, \quad \chi_{-l} = \chi_l. \quad (2.28)$$

241 Only the non-negative Fourier components are necessary to be computed. The symmetric
242 forcing (2.10) imposes the boundary condition

$$243 \quad \psi_l = \frac{d\psi_l}{d\varrho} = 0, \quad \chi_l = i\delta_{0,l} \quad \text{at} \quad \varrho = \eta \quad \text{or} \quad 1. \quad (2.29)$$

244 Note that the forcing is imposed at $l = 0$. Therefore, the following Fourier components are
245 excited

$$246 \quad \chi_0, \psi_1, \chi_2, \psi_3, \dots \quad (2.30)$$

247 On the other hand, the antisymmetric forcing (2.11) imposes the boundary condition

$$248 \quad \psi_l = \frac{d\psi_l}{d\varrho} = 0, \quad \chi_l = i\frac{\varrho}{2} \delta_{1,l} \quad \text{at} \quad \varrho = \eta \quad \text{or} \quad 1. \quad (2.31)$$

249 Note that the forcing is imposed at $l = 1$. Therefore, the following Fourier components are
250 excited

$$251 \quad \chi_1, \psi_2, \chi_3, \psi_4, \dots \quad (2.32)$$

252 As in the 3D configuration, the equations are truncated at the Fourier component L and the
253 derivatives to ϱ are replaced by the Chebyshev differentiation matrices with the order $N + 1$.
254 The resulting block tridiagonal system is solved by the same block tridiagonal algorithm as
255 before.

256 The verification of the two spectral codes used in this paper can be found in Appendix A.

257 3. Wave beams from the critical latitude on the inner core

258 The aforementioned forcings are imposed on the inner core. The forcing frequency ω is chosen
 259 in the inertial range such that inertial waves propagate at an inclined angle $\theta_c = \arccos \omega/2$
 260 relative to the horizontal plane. As in HFRL22, two concentrated wave beams are expected to
 261 be generated from the critical latitude localised at $(r, z) = (\eta\sqrt{1 - \omega^2/4}, \eta\omega/2)$ on the inner
 262 core. These wave beams travel along the tangential line at the critical latitude in two opposite
 263 directions (northward and southward) and reflect on the boundaries and form a ray pattern
 264 in the spherical shell geometry. In general, for a fixed inclined angle θ_c , any ray pattern is
 265 composed of the four rays with opposite propagation directions, which are referred to as the
 266 northward, outward, southward and inward, as shown in figure 2. In HFRL22, we considered
 267 the case where the ray pattern is a simple periodic pattern. Here, we consider a more general
 268 situation where the wave beams converge towards an attractor. Our first objective is to analyse
 269 whether an asymptotic solution can be constructed by propagating the self-similar solution
 270 describing the concentrated wave beam emitted from the critical latitude, as it was done in
 271 HFRL22.

272 In §3.1, the asymptotic theory is presented. The properties of the self-similar solution and
 273 of the reflection laws are first recalled and adapted to the 2D configurations that we also
 274 consider before analysing the propagation towards the attractor. The asymptotic solution is
 275 then compared to numerical results in §3.2.

276 3.1. Asymptotic theory

277 3.1.1. Viscous self-similar solution and scaling

278 The concentrated ray beams emitted from the critical latitude are associated with an inviscid
 279 singularity along the critical ray (Le Dizès 2023). It is the viscous smoothing of this
 280 singularity that gives rise in the limit of small Ekman numbers to a self-similar expression
 281 for the dominant wave beam velocity components (Moore & Saffman 1969).

282 The natural way to describe this self-similar solution is to introduce the local coordinates
 283 $(x_{\parallel}, x_{\perp})$ on the critical ray path, with x_{\parallel} measuring the travelled distance from the source
 284 along the critical ray and x_{\perp} measuring the displacement relative to the critical ray ($x_{\perp} = 0$
 285 is the critical ray equation). The orientation of x_{\perp} is chosen as indicated in figure 2. It is
 286 assumed not to change during the beam propagation.

287 The wave beam is centred on the critical ray and has a width of order $E^{1/3}$. In the (r, z)
 288 plane, its main velocity component is oriented along \mathbf{e}_{\parallel} and can be written at leading order
 289 in $E^{1/3}$ in the 3D axisymmetric geometry as (see details in Le Dizès & Le Bars 2017)

$$290 \quad v_{\parallel} = \frac{1}{\sqrt{r}} C_0 H_m(x_{\parallel}, x_{\perp}) = \frac{1}{\sqrt{r}} C_0 \left(\frac{x_{\parallel}}{2 \sin \theta_c} \right)^{-m/3} h_m(\zeta) \quad (3.1)$$

291 with the similarity variable

$$292 \quad \zeta = x_{\perp} E^{-1/3} \left(\frac{2 \sin \theta_c}{x_{\parallel}} \right)^{1/3} \quad (3.2)$$

293 and the special function introduced by Moore & Saffman (1969)

$$294 \quad h_m(\zeta) = \frac{e^{-im\pi/2}}{(m-1)!} \int_0^{+\infty} e^{ip\zeta - p^3} p^{m-1} dp. \quad (3.3)$$

295 The parameters C_0 and m denote the amplitude and singularity strength respectively, which
 296 will be specified below. Note that this meaning of m should not be confused with the order of
 297 the spherical harmonics in the spectral expansion (2.13), which is not used here since we focus

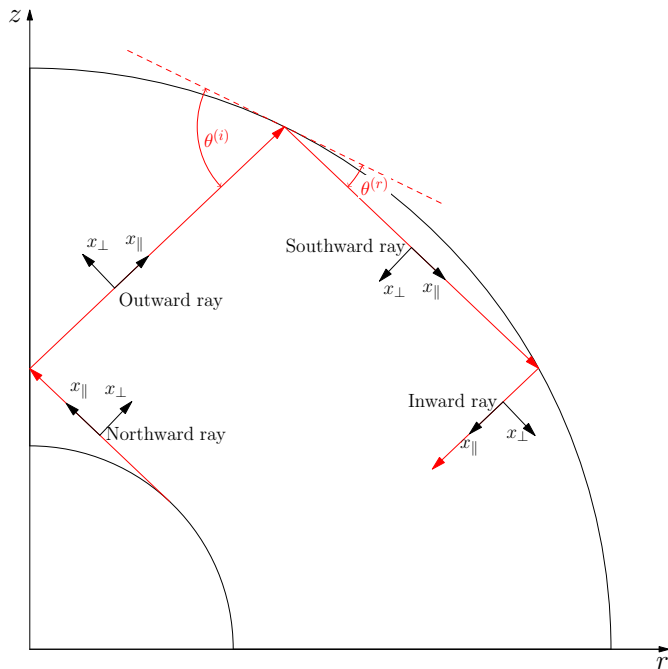


Figure 2: Four propagation directions of the rays in a closed domain. The local vectors attached to each ray are the orientations of the local frames $(x_{\parallel}, x_{\perp})$.

298 on purely axisymmetric solutions. The velocity across the critical rays v_{\perp} and the pressure p
 299 are $O(E^{1/3})$ smaller. However, the wave beam has a velocity component normal to the (r, z)
 300 plane of same order which is given by (see Rieutord *et al.* 2001; Le Dizès & Le Bars 2017)

$$301 \quad v_{\phi} = \pm i v_{\parallel}. \quad (3.4)$$

302 The sign corresponds to the sign of the projection of the local unit vector e_{\parallel} onto the global
 303 unit vector e_r . For the northward and inward rays, the sign is $-$; for the southward and
 304 outward rays, the sign is $+$ (see figure 2).

305 The inviscid singularity that gives rise to the self-similar viscous solution is recovered by
 306 taking the limit $\zeta \rightarrow \infty$ in (3.1)

$$307 \quad v_{\parallel} \rightarrow \frac{1}{\sqrt{r}} C_0 x_{\perp}^{-m} E^{m/3} \quad \text{as } \zeta \rightarrow +\infty. \quad (3.5)$$

As we shall see, it is also useful to introduce the streamfunction ψ that can be defined for axisymmetric flows by

$$v_{\parallel} = \epsilon \frac{1}{r} \frac{\partial \psi}{\partial x_{\perp}}, \quad v_{\perp} = -\epsilon \frac{1}{r} \frac{\partial \psi}{\partial x_{\parallel}}, \quad (3.6a, b)$$

308 where $\epsilon = 1$ for the rays propagating northward and southward and $\epsilon = -1$ for the rays
 309 propagating inward and outward (see figure 2). Equation (3.6a) can be integrated to give at
 310 leading order

$$311 \quad \psi = \epsilon \sqrt{r} \frac{C_0 E^{1/3}}{m-1} H_{m-1}(x_{\parallel}, x_{\perp}). \quad (3.7)$$

312 Note that the streamfunction ψ is $E^{1/3}$ smaller than the parallel velocity v_{\parallel} .

The above expressions are valid for 3D axisymmetric geometries. For 2D configurations,

	3D libration	2D symmetric forcing	2D antisymmetric forcing
$\frac{8(2 \sin \theta_c)^{1/2} (2/\eta)^{1/4} C_0 }{E^{1/12}}$	$(\eta \sin \theta_c)^{3/2}$	1	$\eta \sin \theta_c$

Table 1: Absolute value of the complex amplitude C_0 for different forcings.

the term \sqrt{r} is not present in the velocity and streamfunction expressions. We get

$$v_{\parallel}^{(2D)} = C_0 H_m(x_{\parallel}, x_{\perp}), \quad (3.8a)$$

$$\psi^{(2D)} = \epsilon \frac{C_0 E^{1/3}}{m-1} H_{m-1}(x_{\parallel}, x_{\perp}). \quad (3.8b)$$

313 The velocity component v_y , perpendicular to the (x, z) plane differs from $v_{\parallel}^{(2D)}$ by a $\pm\pi/2$
 314 phase factor, as the relation (3.4) between v_{ϕ} and v_{\parallel} in 3D.

315 In the self-similar solution (3.1), the free parameters, the singularity strength m and
 316 the amplitude C_0 , depend on the nature of the forcing. For a viscous forcing, that is a
 317 forcing induced by Ekman pumping, these parameters can be obtained in closed form for the
 318 northward and southward beams generated from the critical latitude (Le Dizès & Le Bars
 319 2017; Le Dizès 2023). For a librating sphere, they are given by (Le Dizès & Le Bars 2017)

$$320 \quad m = 5/4, \quad (3.9)$$

and

$$C_0 = \frac{E^{1/12}}{8(2 \sin \theta_c)^{1/2} (2/\eta)^{1/4}} e^{i\pi/2} \quad \text{for the northward beam,} \quad (3.10a)$$

$$C_0 = \frac{E^{1/12}}{8(2 \sin \theta_c)^{1/2} (2/\eta)^{1/4}} e^{i3\pi/4} \quad \text{for the southward beam.} \quad (3.10b)$$

321 These expressions can be applied to our geometry for the three forcings (2.6, 2.10 and
 322 2.11) imposed on the inner core. Considering the different non-dimensionalisation of lengths
 323 adopted by Le Dizès & Le Bars (2017) and this work (the radial distance of the critical
 324 latitude to the rotation axis vs the outer radius), the absolute value of the complex amplitude
 325 C_0 should be adapted as indicated in table 1 for the three forcings. The factor $\eta \sin \theta_c$ is the
 326 distance of the critical latitude to the axis Oz .

327 Note that the amplitude C_0 of the parallel velocity scales as $E^{1/12}$. This scaling has
 328 been validated by HFRL22 for Ekman numbers down to 10^{-10} . The amplitude of the
 329 streamfunction is weaker and of order $E^{5/12}$.

330 3.1.2. Reflections on the boundaries and on the axis

The reflection of a self-similar wave beam on a boundary has been discussed in Le Dizès
 (2020) and HFRL22. Le Dizès (2020) showed that the wave beam keeps its self-similar
 form when it reflects on a boundary. More precisely if the incident beam is written as
 $v_{\parallel}^{(i)} = C_0^{(i)} H_m(x_{\parallel}^{(i)}, x_{\perp}^{(i)})$, the reflected beam can also be written as $v_{\parallel}^{(r)} = C_0^{(r)} H_m(x_{\parallel}^{(r)}, x_{\perp}^{(r)})$
 with

$$\frac{x_{\parallel b}^{(r)}}{x_{\parallel b}^{(i)}} = \alpha^3, \quad \frac{C_0^{(r)}}{C_0^{(i)}} = \alpha^{m-1}, \quad (3.11a, b)$$

331 where the subscript b indicates values taken at the reflection point. The reflection factor α
332 at the reflection point is given by

$$333 \quad \alpha = \frac{\sin \theta^{(r)}}{\sin \theta^{(i)}} \quad (3.12)$$

334 where $\theta^{(r)}$ and $\theta^{(i)}$ are the angles of the reflected and incident beams with respect to the
335 boundary (see figure 2). This factor is smaller than 1 (resp. larger than 1) when there is a
336 contraction (resp. expansion) of the beam. A reflection on a boundary then just modifies the
337 travelled distance from the source and the amplitude of the beam. In particular it has no effect
338 on its phase.

339 Note however that this reflection law implicitly assumes that the beam is not forced at the
340 boundary where it reflects. This in particular implies a simple relation on the streamfunction
341 of the incident and reflected beams at the boundary that can be written as

$$342 \quad \psi^{(r)}(x_{\parallel b}^{(r)}, x_{\perp b}^{(r)}) + \psi^{(i)}(x_{\parallel b}^{(i)}, x_{\perp b}^{(i)}) = 0. \quad (3.13)$$

343 We shall see below that this relation is no longer valid when we get very close to an attractor.

The crossing of the wave beam with the rotation axis is of different nature. In the 3D
axisymmetric geometry, the self-similar solution diverges on the axis, but it can nevertheless
be continued as if there was a reflection. The relation between the incident and reflected
beams is obtained by a condition of matching with the solution obtained close to the axis (see
Le Dizès & Le Bars 2017). We obtain in that case a phase shift of $\pi/2$ between the reflected
and incident beams:

$$x_{\parallel b}^{(r)} = x_{\parallel b}^{(i)}, \quad C_0^{(r)} = e^{i\varphi} C_0^{(i)}, \quad (3.14a, b)$$

344 with $\varphi = \pi/2$.

In the 2D configurations, the condition of reflection to apply on the axis Oz is directly
related to the property of symmetry of the forcing. On the axis Oz , the projections of
propagation directions of the incident and reflected rays onto the global unit vector \mathbf{e}_x are of
opposite sign. According to the formula (3.4), we then have the following relations

$$v_y^{(r)} = \pm i v_{\parallel}^{(r)}, \quad v_y^{(i)} = \mp i v_{\parallel}^{(i)}. \quad (3.15a, b)$$

345 For the 2D symmetric forcing (2.10) where v_y is forced in a symmetric way about the axis
346 Oz , we have $v_y^{(r)} = v_y^{(i)}$. Therefore, the parallel velocities are of opposite sign, which means

$$347 \quad \varphi = \pi, \quad (3.16)$$

348 in (3.14). For the 2D antisymmetric forcing (2.11) with $v_y^{(r)} = -v_y^{(i)}$, the parallel velocity is
349 unchanged which means that

$$350 \quad \varphi = 0. \quad (3.17)$$

351 In order to consider a quarter of the domain in the (r, z) or (x, z) plane, the horizontal axis
352 Or (or Ox) has also to be considered as a place of reflection. Applying the same approach,
353 we can easily show that no phase shift is created between reflected and incident beams on
354 this axis for all the three forcings.

355 3.1.3. Propagation of critical-latitude beams

356 Having provided the structure of the wave beam and how it reflects on the boundaries and the
357 axis, we are now in a position to analyse its propagation in a closed geometry. As explained
358 above, we consider a frequency such that the rays emitted from the critical latitude on the
359 inner core end up on an attractor. Our objective is to obtain the property of the self-similar
360 beam centred on the critical ray as it moves towards the attractor. An example of critical ray

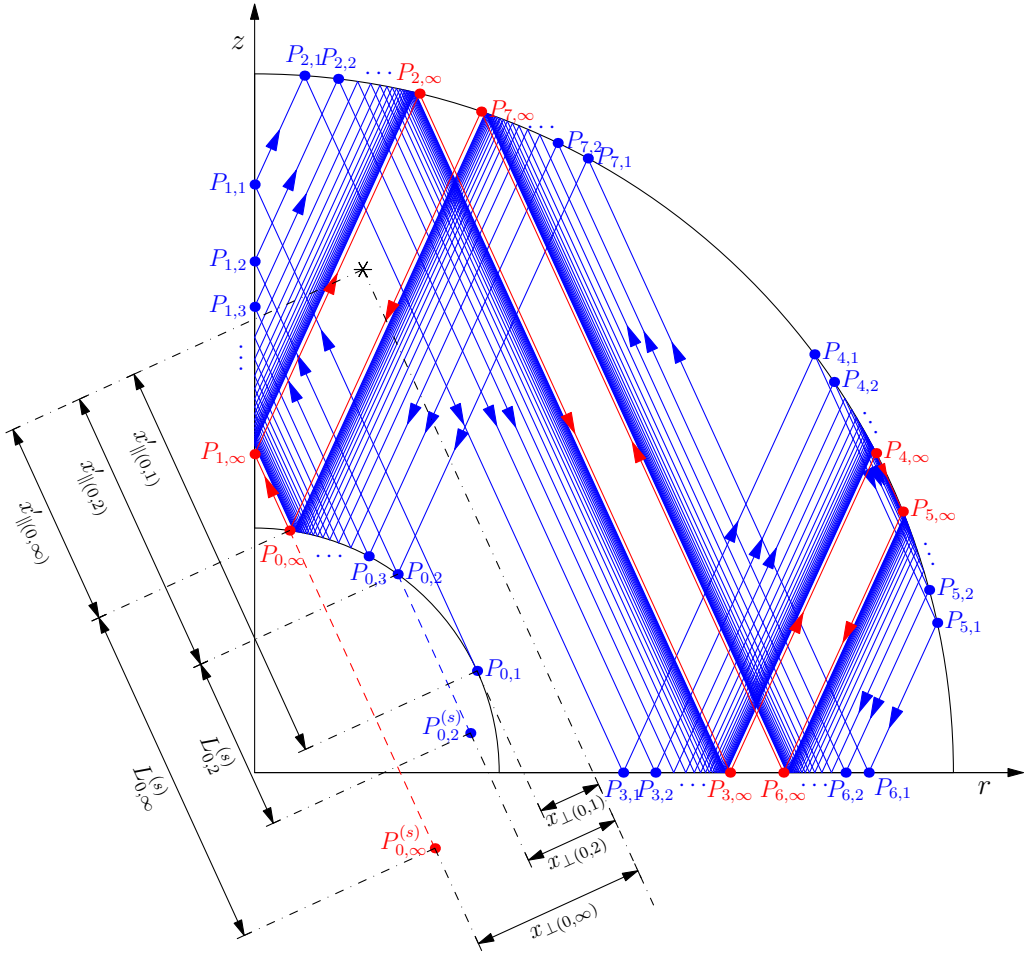


Figure 3: Schematic of propagation of a critical ray towards an attractor for $\eta = 0.35$ and $\omega = 0.8317$. The symbol * denotes an arbitrary point, from which the local coordinates of each segment $(0, n)$ are measured.

361 is shown in figure 3 where the ray (blue lines) propagates northward from the critical latitude
 362 and spirals into one side of the attractor (red lines). In the following, we use this figure for
 363 explanation purposes but the methodology is applicable for any type of wave patterns.

364 The reflection positions on the axes and the boundaries during every loop are indicated as
 365 $P_{j,n}$, where j denotes the reflection position and ranges from 0 to $J-1$ ($J = 8$ in figure 3). The
 366 index n denotes the number of the cycle and ranges from 1 to ∞ . For example, the reflection
 367 points on the rotation axis are $P_{1,1}, P_{1,2}, \dots$ and $P_{1,\infty}$. To simplify the formula we assume
 368 that the initial point of a cycle is the position J of the former cycle, that is $P_{0,n+1} = P_{J,n}$.
 369 The critical latitude corresponds to $P_{0,1}$. The critical ray follows the following path during
 370 propagation

$$371 \quad P_{0,1}P_{1,1} \cdots P_{J-1,1} \rightarrow P_{0,2}P_{1,2} \cdots P_{J-1,2} \rightarrow \cdots \rightarrow P_{0,\infty}P_{1,\infty} \cdots P_{J-1,\infty}. \quad (3.18)$$

372 The critical ray ends up on the attractor denoted by $P_{0,\infty}P_{1,\infty} \cdots P_{J-1,\infty}$ after an infinite
 373 number of cycles.

374 The solution obtained by propagating the self-similar beam along the critical ray is

375 expected to be composed of as many contributions as the number of segments between
 376 two reflection points. We use the subscript (j, n) to denote the parameters associated with
 377 the segment $P_{j,n}P_{j+1,n}$ (with j between 0 and $J - 1$). Finding the parameters characterising
 378 this contribution requires tracking the variation of the travelled distance and of the amplitude
 379 during all the previous reflections. For this purpose, it is useful to write the travelled distance
 380 $x_{\parallel(j,n)}$ as

$$381 \quad x_{\parallel(j,n)} = L_{j,n}^{(s)} + x'_{\parallel(j,n)} \quad (3.19)$$

382 where $x'_{\parallel(j,n)}$ is the distance from $P_{j,n}$ and $L_{j,n}^{(s)}$ is the distance of the “virtual” source $P_{j,n}^{(s)}$
 383 from $P_{j,n}$. The condition of reflection (3.11) applied in $P_{j+1,n}$ implies that

$$384 \quad L_{j+1,n}^{(s)} = (L_{j,n}^{(s)} + L_{j,n})\alpha_{j+1,n}^3, \quad (3.20)$$

385 where $L_{j,n}$ is the length of the segment (j, n) and $\alpha_{j+1,n}$ is the reflection factor at $P_{j+1,n}$.
 386 Concerning the amplitude $C_{j,n}$ of the self-similar solution, we obtain from (3.11b) with (3.9)

$$387 \quad C_{j+1,n} = C_{j,n}\alpha_{j+1,n}^{1/4} e^{i\varphi_{j+1}}, \quad (3.21)$$

388 where φ_j is the phase shift obtained at the reflection at $P_{j,n}$. For the critical ray shown in
 389 figure 3, this phase shift is null except for $j = 1$ (because the reflection is on the axis), for
 390 which it can be either $\pi/2$ (3D case), π (2D symmetric case) or 0 (2D antisymmetric case).

391 In the following, we shall consider the solution in a section perpendicular to the segments
 392 $(0, n)$. It is therefore useful to consider the evolution of the beam after each cycle for this
 393 particular segment as a function of n . Using (3.20), we can write

$$394 \quad L_{0,n+1}^{(s)} \equiv L_{J,n}^{(s)} = (L_{0,n}^{(s)} + \Lambda_n)\alpha_n^3, \quad (3.22)$$

395 with

$$396 \quad \Lambda_n = L_{0,n} + \frac{L_{1,n}}{\alpha_{1,n}^3} + \frac{L_{2,n}}{\alpha_{1,n}^3 \alpha_{2,n}^3} + \cdots + \frac{L_{J-1,n}}{\alpha_{1,n}^3 \alpha_{2,n}^3 \cdots \alpha_{J-1,n}^3}, \quad (3.23)$$

397 and

$$398 \quad \alpha_n = \alpha_{1,n}\alpha_{2,n} \cdots \alpha_{J,n}. \quad (3.24)$$

399 Similarly, we obtain

$$400 \quad C_{0,n+1} \equiv C_{J,n} = C_{0,n}\alpha_n^{1/4} e^{i\varphi}, \quad (3.25)$$

401 with

$$402 \quad \varphi = \varphi_1 + \varphi_2 + \cdots + \varphi_J. \quad (3.26)$$

403 Note that $\alpha_{J,n} = \alpha_{0,n+1}$ and $\varphi_J = \varphi_0$. For the first segment of the first cycle, the source is at
 404 $P_{0,1}$, so $L_{0,1} = 0$ and the amplitude $C_{0,1}$ is given by the expression (3.10) of C_0 .

405 Although a given parameter $\alpha_{j,n}$ can be larger than 1, the product (3.24) that defines α_n is
 406 necessarily smaller than 1 (for n sufficiently large) because the critical ray converges toward
 407 an attractor. Its limit value α_∞ corresponds to the contraction factor of the attractor. The
 408 amplitude of the beam therefore goes rapidly to zero as one gets close to the attractor. This
 409 guarantees that, although the various contributions superimpose on each other close to the
 410 attractor, the sum will remain finite on the attractor. The expression obtained by summing all
 411 the contributions coming from the segments $(0, n)$ with n ranging from 1 to ∞ is then well
 412 defined. It can be written as

$$413 \quad v_{\parallel} \sim \sum_{n=1}^{\infty} v_{\parallel(0,n)} \quad , \quad \psi \sim \sum_{n=1}^{\infty} \psi_{0,n} \quad (3.27)$$

414 for the parallel velocity and the streamfunction respectively. These expressions are expected
 415 to provide an asymptotic solution close to segments $(0, n)$. In the following, they will be
 416 referred to as the critical-latitude solution. In the next section, they are plotted and compared
 417 to numerical solutions.

418

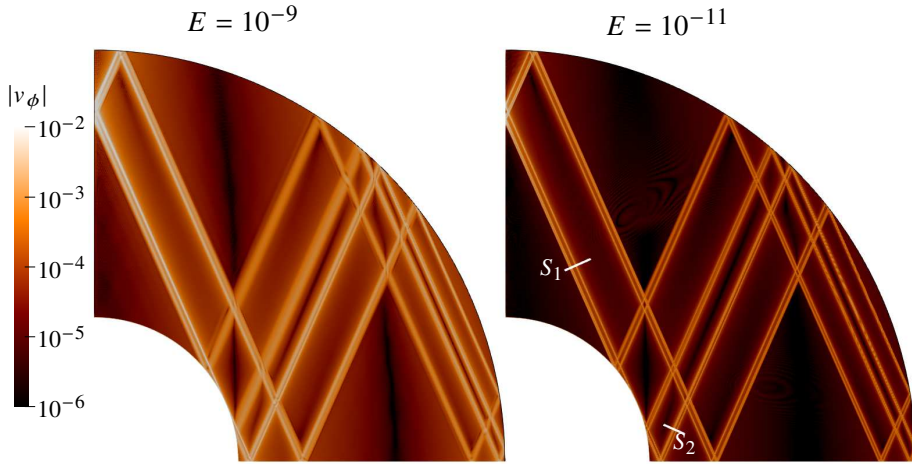
3.2. Results

419 The numerical solutions are obtained for Ekman numbers as low as 10^{-11} for which the scale
 420 separation between the wave beams and the domain size is clear. For simplicity, the velocity
 421 components v_ϕ in 3D and v_y in 2D are used for comparison. Other velocity components
 422 follow a similar trend.

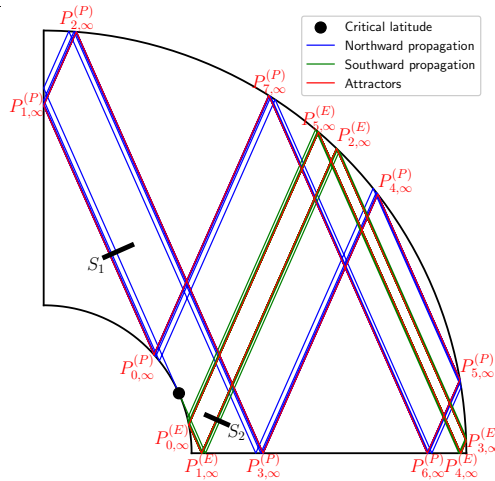
423 We consider the wave pattern with two coexisting attractors in a spherical shell as discussed
 424 by Tilgner (1999) and Rieutord *et al.* (2001). The aspect ratio and the frequency for this case
 425 are $\eta = 0.35$ and $\omega = 0.8102$ respectively. The forcing is imposed on the inner core. The
 426 numerical results of the 3D libration at $E = 10^{-9}$ and $E = 10^{-11}$ illustrated by the amplitude
 427 of v_ϕ are shown in figure 4a. The wave beams at the lower Ekman number are more separated.
 428 The wave pattern is consistent with the ray paths from the critical latitude on the forced inner
 429 core (see figure 4b). The ray propagating northward from the critical latitude (in blue color)
 430 converges onto the polar attractor $P_{0,\infty}^{(P)} \cdots P_{7,\infty}^{(P)}$, while that propagating southward from the
 431 critical latitude (in green color) converges onto the equatorial attractor $P_{0,\infty}^{(E)} \cdots P_{5,\infty}^{(E)}$. The
 432 corresponding 2D results are not shown because the ray paths are identical and the wave
 433 pattern qualitatively similar for the same aspect ratio and frequency. However, one should
 434 note that the phase shift φ varies for different attractors and forcings. For the polar attractor
 435 with one vertex on the axis Oz , the phase shifts are $\pi/2$, π and 0 for the 3D libration, 2D
 436 symmetric and antisymmetric forcings, respectively. For the equatorial attractor, there is no
 437 phase shift for any of the forcing as this attractor does not touch the axis Oz .

438 Two cuts crossing the two attractors are chosen in order to validate the critical-latitude
 439 asymptotic solution given by equation (3.27). Figures 5 and 6 compare the velocity profiles
 440 between the asymptotic solutions and the numerical solutions at $E = 10^{-11}$ on the cuts S_1
 441 and S_2 respectively (see figure 4). The cut S_1 on the polar attractor is only crossed by the ray
 442 propagating northward from the critical latitude (blue lines in figure 4b), while the cut S_2 on
 443 the equatorial attractor is only crossed by the ray propagating southward (green lines in figure
 444 4b). In figures 5 and 6, the vertical lines show the positions of the northward and southward
 445 critical rays when they cross S_1 and S_2 respectively. These critical positions correspond to
 446 different successive loops. From the rightmost critical position (r_1) to the leftmost one (r_∞),
 447 the critical ray propagates from the first loop ($n = 1$) to the final loop ($n = \infty$) and from
 448 the critical latitude to the final attractor. The critical-latitude solutions on these two cuts S_1
 449 and S_2 are built by propagating the self-similar solutions from the critical latitude northward
 450 and southward respectively, by using the infinite sum of self-similar solutions (3.27); see the
 451 dashed lines in figures 5 and 6 respectively. Since the amplitude decreases exponentially the
 452 summation is conducted to a large enough number of loops in order to ensure convergence
 453 (around 150 loops in practice). The amplitudes are rescaled according to table 1, in order to
 454 make sure that the wave beams from the critical latitude possess the same amplitudes for all
 455 the three forcings. Note that the radial dependence of the 3D configuration is removed by
 456 multiplying the velocity with \sqrt{r} .

457 Around the first critical position r_1 , the wave beam from the critical latitude is within the
 458 first loop and has not experienced any contraction or expansion on the boundaries. It takes the
 459 same shape for all the three forcings and the self-similar solution agrees with the numerical
 460 solution very well for both two cuts and all the three forcings, as shown by the profiles around
 461 r_1 in figures 5 and 6. After one loop, the wave beam moves on to the next critical position



(a) Numerical results of the amplitude of v_ϕ at $E = 10^{-9}$ and $E = 10^{-11}$.



(b) Ray paths from the critical latitude on the inner core.

Figure 4: Results corresponding to the 3D libration of the inner core for $\eta = 0.35$ and $\omega = 0.8102$.

462 r_2 . The amplitude decreases as expected from the relation (3.25) for $\alpha_n < 1$. The agreement
 463 between the self-similar solution and the numerical solution is still good; see the profiles
 464 around r_2 in figures 5 and 6. However, its shape is now dependent on the phase shift it has
 465 experienced during the first loop. For the polar attractor on S_1 , the profile around r_2 changes
 466 compared to that around r_1 for the 3D libration and 2D symmetric forcing since there is a
 467 nonzero phase shift for both these cases (see figures 5(abcd)). The profiles between r_1 and r_2
 468 remain similar for the 2D antisymmetric forcing since there is no phase shift (figure 5(ef)).
 469 For the equatorial attractor on S_2 , there is no phase shift and the profiles remain similar from
 470 r_1 to r_2 as shown in figure 6 for all the three forcings. A similar behaviour can be observed
 471 from the critical position r_2 to the next position r_3 . Interestingly, as shown in figure 6, the
 472 equatorial attractor profiles on S_2 , which do not cross the rotation axis and therefore do
 473 not alter the phase, are almost the same for all forcing types, after rescaling the amplitudes

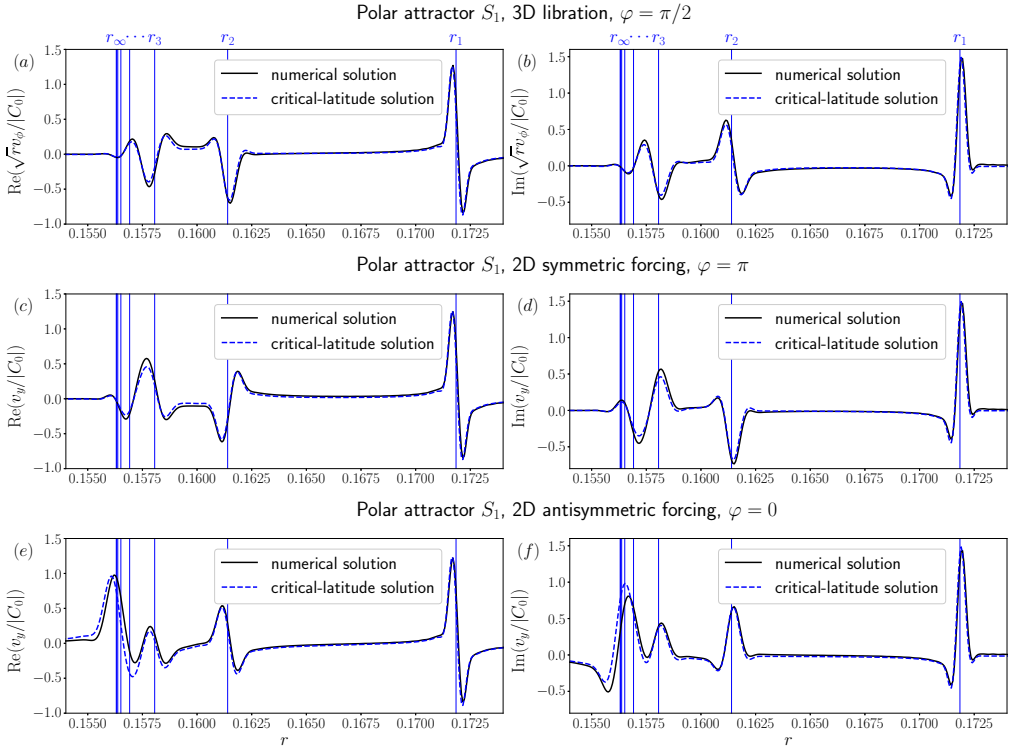


Figure 5: Comparison of velocity profiles between the critical-latitude asymptotic solutions and the numerical solutions on the cut S_1 of the polar attractor shown in figure 4 at $E = 10^{-11}$ for three forcings: (ab) 3D libration (phase shift $\varphi = \pi/2$); (cd) 2D symmetric forcing (phase shift $\varphi = \pi$); (ef) 2D antisymmetric forcing (no phase shift). (ace) are the real parts; (bdf) are the imaginary parts. Amplitudes are rescaled by the expressions of $|C_0|$ in table 1.

474 according to table 1. This is another confirmation that these cases should be describable by
475 a unique theory.

476 When the wave beam moves on to the position of the attractor (r_∞), successive critical
477 positions become very close to each other and the profiles from different loops are not well
478 separated. Finally, the wave beam just propagates on the attractor and the summation of the
479 self-similar solutions is conducted there. As shown by the profiles around the positions of
480 the attractors r_∞ in figures 5 and 6, the attractor with phase shift (figure 5(abcd)) is weaker
481 than that without phase shift (figures 5(ef) and 6). This phenomenon can be explained by
482 the summation of the self-similar solutions on the attractor. When there is a phase shift on
483 the attractor path, the self-similar solutions of successive loops with different phases cancel
484 out, which makes the local solution in the vicinity of the attractor negligible after summation.
485 Otherwise, the self-similar solutions with the same phase accumulate on the attractor, which
486 makes the solution much stronger. For the polar attractor with phase shift (r_∞ in figure
487 5(abcd)), the critical-latitude solution (3.27) is consistent with the numerical solution.
488 However, for the polar attractor without phase shift (r_∞ in figure 5(ef)), the asymptotic
489 solution does not perform as well as for the positions far from the attractor. This deviation is
490 much more obvious for the equatorial attractor without phase shift (r_∞ in figure 6), where the
491 amplitudes are largely overestimated and the critical-latitude solution (3.27) deviates from
492 the numerical solutions gradually as the ray converges towards the attractor.

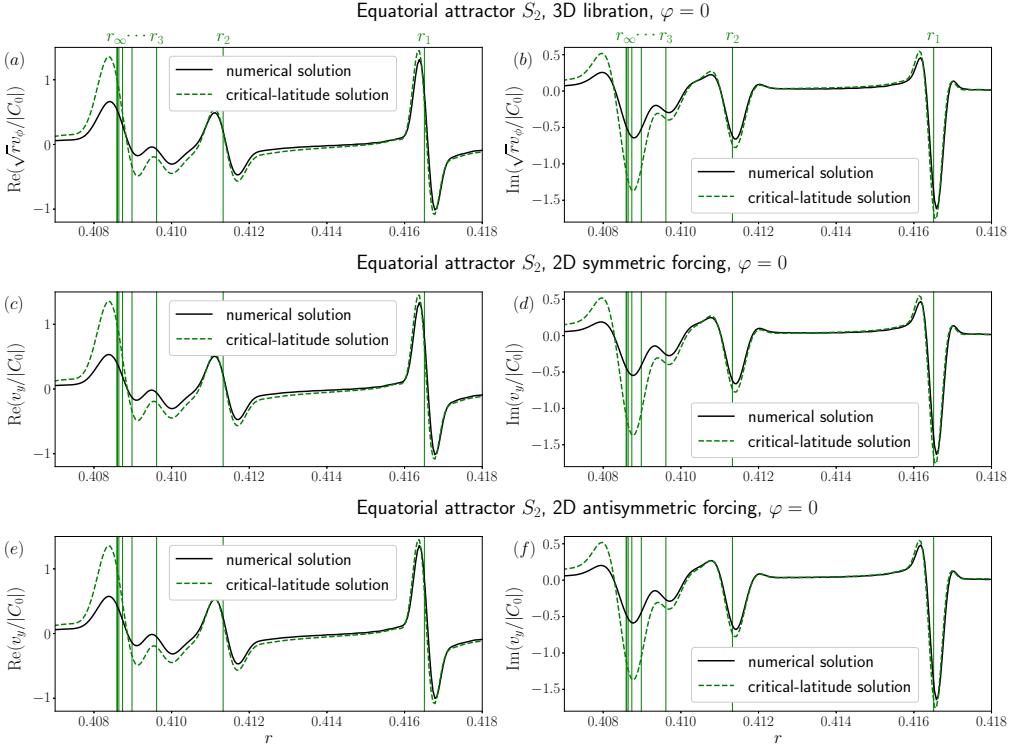


Figure 6: Same caption as in figure 5 but on the cut S_2 of the equatorial attractor. There is no phase shift for all three forcings.

493 In order to investigate what is happening around the attractor, the velocity amplitude
 494 scalings with Ekman number of both the critical-latitude asymptotic solution (3.27) and
 495 the numerical solution at the critical positions on the cuts S_1 and S_2 are shown in figure 7
 496 for the 3D libration. Similar behaviour can be observed for the other two forcings and are
 497 not shown here. The critical-latitude solution (3.27) and the numerical solution at the first
 498 critical position r_1 follow the expected scaling $E^{1/12}$, which validates the Ekman number
 499 scaling of the wave beams from the critical latitude for a libration frequency different from
 500 that in HFRL22. Then the amplitude on S_1 (polar attractor with phase shift) decreases to
 501 a weaker level as the ray gets closer to the position of the attractor r_∞ and the scaling is
 502 eventually closer to $E^{1/6}$. The scaling $E^{1/6}$ around r_∞ is more obvious for the other cut
 503 S_2 of the equatorial attractor without phase shift. However, the corresponding prefactor is
 504 over-predicted by the critical-latitude solution.

505 The change of scaling of the critical-latitude solution could have been anticipated from
 506 expression (3.25) for its amplitude. We have seen that because $\alpha_n < 1$, the amplitude of the
 507 self-similar beam decreases as it gets closer to the attractor. But the beam has also a finite
 508 width of order $E^{1/3}$, so the contributions obtained from each cycle superimpose on each
 509 other when the critical ray gets at a distance of this order from the attractor. This stops the
 510 decreasing of the amplitude after a number n_s of cycles that can be approximately estimated
 511 by $(\log E^{1/3})/(\log \alpha_\infty)$ which corresponds to the number of contractions needed to go from
 512 1 to $E^{1/3}$ with the contraction factor α_∞ . The amplitude C_{0,n_s} has then decreased from its
 513 initial value C_0 by a factor $\alpha_1^{1/4} \alpha_2^{1/4} \dots \alpha_{n_s}^{1/4}$, which is close to $\alpha_\infty^{n_s/4} \approx E^{1/12}$. The velocity

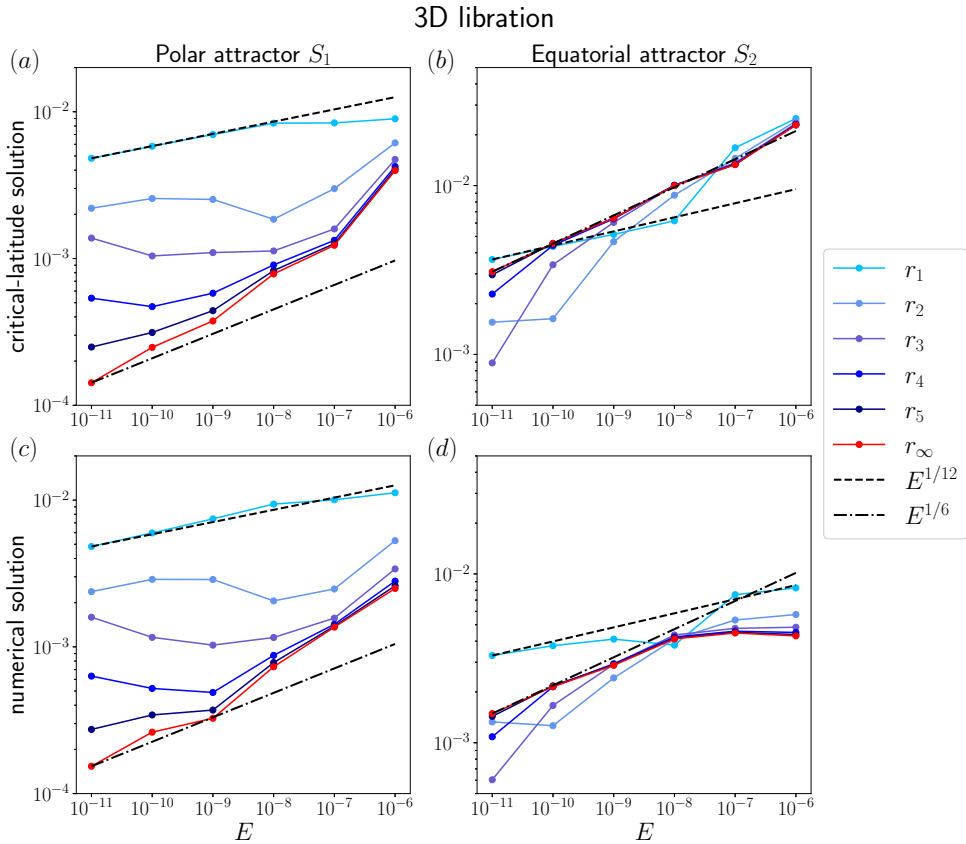


Figure 7: Velocity amplitude scalings of the critical-latitude solution (*ab*) and the numerical solution (*cd*) at the critical positions on the cuts S_1 (*ac*) and S_2 (*bd*) for the 3D libration and at the Ekman numbers $[10^{-11}, 10^{-6}]$. r_1, r_2, \dots and r_∞ are the critical positions shown in figures 5 and 6.

514 amplitude of the critical-latitude solution is therefore expected to become $O(E^{1/12})$ smaller
 515 close to the attractor and therefore of order $E^{1/6}$, as observed.

516 The amplitude of the streamfunction of the critical-latitude solution also decreases from
 517 $O(E^{5/12})$ to $O(E^{1/2})$ as we get close to the attractor. Then, it becomes of the order of the
 518 Ekman pumping (see Appendix B). This means that the hypothesis of no Ekman pumping
 519 that has been used to obtain the reflection laws of the beam in §3.1.2 breaks down. In
 520 particular, relation (3.13) should not be valid close to the attractor. We suspect that the
 521 discrepancies observed close to the attractor between the critical-latitude solution and the
 522 numerical solution are due to this effect.

523 In the next section, we develop a new asymptotic theory to describe the solution close to
 524 the attractor. This theory, that takes into account the Ekman pumping close to the attractor,
 525 is based on ideas originally developed by O05.

526 4. Solution close to the attractors

527

4.1. Asymptotic theory

528 In order to apply the results of O05, we first consider 2D configurations without phase shift
 529 or reflection on the axis. In this framework, the inviscid problem can be solved using the
 530 2D streamfunction only and a global solution for the streamfunction is obtained as a sum of
 531 two functions which are constant along the characteristics of the problem (e.g. Maas & Lam
 532 1995).

533 In the present work, we are looking for a solution localised near an attractor, say
 534 $P_{0,\infty} \cdots P_{j-1,\infty}$ as illustrated in figure 3, which can be written as a sum of local solutions
 535 $\psi_{j,\infty}^{(2D)}(x_{\perp(j,\infty)})$ valid close to the segment (j, ∞) only. In the 2D inviscid framework, these
 536 local solutions just mean that the solution is transported from $P_{j,\infty}$ to $P_{j+1,\infty}$ along the lines
 537 $x_{\perp(j,\infty)} = Cst$ without modification. Whereas the critical-latitude solution was reflected on
 538 boundary without modification, the solution constructed by O05 is directly forced by the
 539 boundary condition in the neighborhood of the attractor. Close to a point $P_{j,\infty}$, the solution
 540 is expected to be composed of the incident solution $\psi_{j,\infty}^{(2D)}(x_{\perp(j,\infty)})$ and of the reflected
 541 solution $\psi_{j+1,\infty}^{(2D)}(x_{\perp(j+1,\infty)})$ and satisfies the boundary condition on the surface :

$$542 \quad \psi_{j,\infty}^{(2D)}(x_{\perp(j,\infty)}) + \psi_{j+1,\infty}^{(2D)}(x_{\perp(j+1,\infty)}) = \psi_{j,\infty}^{(EP)}, \quad (4.1)$$

543 where the condition of being on the surface close to $P_{j,\infty}$ means that

$$544 \quad x_{\perp(j+1,\infty)} = \alpha_{j,\infty} x_{\perp(j,\infty)}. \quad (4.2)$$

545 In (4.1), $\psi_{j,\infty}^{(EP)}$ is the value of the streamfunction prescribed at $P_{j,\infty}$. In our case, this
 546 prescribed value is given by the Ekman pumping at the surface (or is zero if there is no
 547 Ekman pumping).

548 If we apply these conditions at each point $P_{0,\infty}, P_{1,\infty} \cdots P_{j-1,\infty}$ of the attractor, we end
 549 up, after a complete cycle, with an equation for each $\psi_{j,\infty}$ which can be written as

$$550 \quad \psi_{j,\infty}^{(2D)}(\alpha_{\infty} x_{\perp(j,\infty)}) - \psi_{j,\infty}^{(2D)}(x_{\perp(j,\infty)}) = \epsilon_{j,\infty} \delta, \quad (4.3)$$

551 with

$$552 \quad \delta = \sum_{k=1}^{J/2} (\psi_{2k,\infty}^{(EP)} - \psi_{2k+1,\infty}^{(EP)}), \quad (4.4)$$

553 and

$$554 \quad \alpha_{\infty} = \alpha_{1,\infty} \alpha_{2,\infty} \cdots \alpha_{J,\infty}, \quad (4.5)$$

555 where we have used the fact that the point $P_{j+J,\infty}$ corresponds to the point $P_{j,\infty}$ (implying that
 556 $\psi_{j,\infty} = \psi_{j+J,\infty}$ and $\psi_{j+J,\infty}^{(EP)} = \psi_{j,\infty}^{(EP)}$). The parameter $\epsilon_{j,\infty}$ is the sign in the streamfunction
 557 definition (3.6). The parameter α_{∞} is the contraction factor of the attractor. Equation (4.3) is
 558 a functional constraint on the inviscid solution close to a 2D attractor. It is identical to the
 559 equation (3.17) of O05.

560 The general solution of this equation can be written as

$$561 \quad \psi_{j,\infty}^{(2D)}(x_{\perp(j,\infty)}) = \frac{\epsilon_{j,\infty} \delta}{\ln \alpha_{\infty}} \ln |x_{\perp(j,\infty)}| + \sum_{n=-\infty}^{+\infty} h_n^{\pm} |x_{\perp(j,\infty)}|^{\frac{2n\pi i}{\ln \alpha_{\infty}}}, \quad (4.6)$$

562 where the \pm sign is for positive or negative $x_{\perp(j,\infty)}$. Interestingly, the dominant logarithmic
 563 part of this solution has a simple expression that only depends on the contraction factor α_{∞}

564 and the forcing term δ . This part corresponds to a particular solution of (4.3), while the sum
 565 is a general homogeneous solution determined by the global ray mapping. Contrarily to O05,
 566 we shall not try to determine this homogeneous solution, since the global ray mapping for the
 567 attractors in a spherical shell is not expected to be simple. We shall only keep the dominant
 568 logarithmic term to describe the inviscid solution close to the attractor. This hypothesis is not
 569 justified from an asymptotical point of view but O05 showed that the correction associated
 570 with the homogeneous part was very small for his case.

571 If we only keep the particular solution, we then get a simple inviscid expression for the
 572 parallel velocity which is

$$573 \quad v_{\parallel(j,\infty)}^{(2D)} \sim \frac{\delta}{\ln \alpha_\infty} x_{\perp(j,\infty)}^{-1}. \quad (4.7)$$

574 As already explained above, this singular behavior can be smoothed by viscosity by
 575 introducing the self-similar solution of Moore & Saffman. The viscous solution that matches
 576 with the singular behavior (4.7) is

$$577 \quad v_{\parallel(j,\infty)}^{(2D)} \sim C_0^{(A)} H_1(x_{\parallel(j,\infty)}, x_{\perp(j,\infty)}), \quad (4.8)$$

578 with

$$579 \quad C_0^{(A)} = \frac{\delta}{\ln \alpha_\infty} E^{-1/3}, \quad (4.9)$$

580 where $H_m(x_{\parallel}, x_{\perp})$ has been defined in (3.1).

581 In the above expression, the virtual source of the beam, that is the position where $x_{\parallel(j,\infty)} = 0$
 582 is however not known. This position can be obtained by using the argument developed in
 583 §3.1.3 for the critical-latitude solution. In particular, if as above, $x_{\parallel(j,\infty)}$ is written as

$$584 \quad x_{\parallel(j,\infty)} = L_{j,\infty}^{(s)} + x'_{\parallel(j,\infty)} \quad (4.10)$$

585 with $x'_{\parallel(j,\infty)} = 0$ at $P_{j,\infty}$, the distance $L_{j,\infty}^{(s)}$ satisfies equations (3.20) and (3.22) with $n \rightarrow \infty$.
 586 For the first segment between $P_{0,\infty}$ and $P_{1,\infty}$, we then get using (3.22)

$$587 \quad L_{0,\infty}^{(s)} = (L_{0,\infty}^{(s)} + \Lambda_\infty) \alpha_\infty^3, \quad (4.11)$$

588 that is

$$589 \quad L_{0,\infty}^{(s)} = \Lambda_\infty \frac{\alpha_\infty^3}{1 - \alpha_\infty^3}, \quad (4.12)$$

590 where Λ_∞ and α_∞ are given by (3.23) and (3.24) with $n \rightarrow \infty$.

591 It is worth noting that the amplitude of the attractor solution does not change along the
 592 cycle. This is due to the particular value of the index of m of the self-similar solution, that is
 593 $m = 1$ for the attractor solution, which guarantees that the amplitude does not change when
 594 the beam reflects on the boundary, as prescribed by the reflection law (3.11b).

595 For the 3D configurations or when there is a phase shift during a cycle, the above
 596 considerations have to be modified. First note that in 3D axisymmetric geometries, the
 597 streamfunction is not identically propagated along characteristics as it is in 2D. It evolves
 598 according to a propagator defined by the Riemann function, which is a Legendre function of
 599 index $-1/2$ for axisymmetric solutions considered here (but see §2.3.2 of Rieutord *et al.* 2001,
 600 for more details). In other words, there is no simple global expression of the inviscid solution
 601 for the streamfunction in 3D. However, if the solution varies on small scales compared to the
 602 distance to the axis, the propagation is almost as in 2D: in that case, an approximate local

603 solution can be obtained far from the axis in the form

$$604 \quad \psi = \sqrt{r} \tilde{\psi}(x_{\perp}), \quad v_{\parallel} = \frac{\tilde{v}_{\parallel}(x_{\perp})}{\sqrt{r}}, \quad (4.13)$$

605 where the \sqrt{r} factor guarantees that these approximations are valid up to second order
606 corrections. The same analysis as above can then be performed for $\tilde{\psi}$ as long as we are far
607 from the axis. This leads to a 3D expression for the local solution near an attractor without
608 phase shift which is directly obtained from (4.8) as

$$609 \quad v_{\parallel(j,\infty)} \sim \frac{C_0^{(A)}}{\sqrt{r}} H_1(x_{\parallel(j,\infty)}, x_{\perp(j,\infty)}), \quad (4.14)$$

610 with $C_0^{(A)}$ given by (4.9) but with a slightly different expression for δ

$$611 \quad \delta = \sum_{k=1}^{J/2} \left(\frac{\psi_{2k,\infty}^{(EP)}}{\sqrt{r_{2k,\infty}}} - \frac{\psi_{2k+1,\infty}^{(EP)}}{\sqrt{r_{2k+1,\infty}}} \right). \quad (4.15)$$

612 For the solution along the first segment $P_{0,\infty}P_{1,\infty}$, $x_{\parallel(j,\infty)}$ is still defined by (4.10) and (4.12).

613 For the attractor without reflection on the axis, it is the expressions (4.8) for 2D
614 configurations and (4.14) for 3D configurations that we shall use and compare to our
615 numerical data.

616 We now want to consider the case of an attractor touching the axis. For the critical-latitude
617 solution, we have seen that a phase shift could be generated as the beam reflects on the axis.
618 A similar phenomenon is expected for the attractor solution. Let us first consider the 2D
619 configurations. We have seen that in that case, the presence of a phase shift depends on the
620 symmetry of the forcing with respect to the z axis. A phase shift of $\varphi = \pi$ is expected for
621 a symmetric forcing, while no phase shift is present for an antisymmetric forcing. This is
622 easily understood as changing x into $-x$ changes $x_{\perp(0,\infty)}$ into $x_{\perp(1,\infty)}$. The local solutions
623 $\psi_{0,\infty}^{(2D)}(x_{\perp(0,\infty)})$ and $\psi_{1,\infty}^{(2D)}(x_{\perp(1,\infty)})$, valid close to the two lines $x_{\perp(0,\infty)} = 0$ and $x_{\perp(1,\infty)} = 0$
624 respectively, should therefore satisfy the same symmetry as the forcing, that is,

$$625 \quad \psi_{1,\infty}^{(2D)}(x_{\perp(1,\infty)}) = \psi_{0,\infty}^{(2D)}(x_{\perp(0,\infty)}) \quad (4.16)$$

626 for the symmetric forcing and

$$627 \quad \psi_{1,\infty}^{(2D)}(x_{\perp(1,\infty)}) = -\psi_{0,\infty}^{(2D)}(x_{\perp(0,\infty)}) \quad (4.17)$$

628 for the antisymmetric forcing, when $x_{\perp(0,\infty)} = x_{\perp(1,\infty)}$. For the antisymmetric case, the axis
629 is therefore as a vertical boundary without Ekman pumping [compare (4.17) to (4.1)]. The
630 same solution as for a 2D attractor not reflecting on the axis can therefore be used. For the
631 symmetric case, this is no longer the case. Owing to (4.16), (4.3) now becomes

$$632 \quad \psi_{j,\infty}^{(2D)}(\alpha_{\infty} x_{\perp(j,\infty)}) + \psi_{j,\infty}^{(2D)}(x_{\perp(j,\infty)}) = \epsilon_{j,\infty} \delta, \quad (4.18)$$

633 if there is an even number of reflections on the axis. A particular solution to this equation is
634 just $\psi_{j,\infty}^{(2D)}(x_{\perp(j,\infty)}) = \epsilon_{j,\infty} \delta / 2$ so there is no logarithmic singularity in the solution anymore.

635 Thus, the inviscid expression (4.7) is not obtained, neither its viscous counterpart (4.8).

636 In 3D, as a phase shift of $\pi/2$ appears when the ray reflects on the axis, a similar
637 phenomenon is expected if the number of reflections on the axis is not a multiple of 4. In
638 that case, no logarithmic singularity should be present in the function $\tilde{\psi}_{j,\infty}$, and the analysis
639 performed above should also break down. A weaker attractor solution is probably obtained

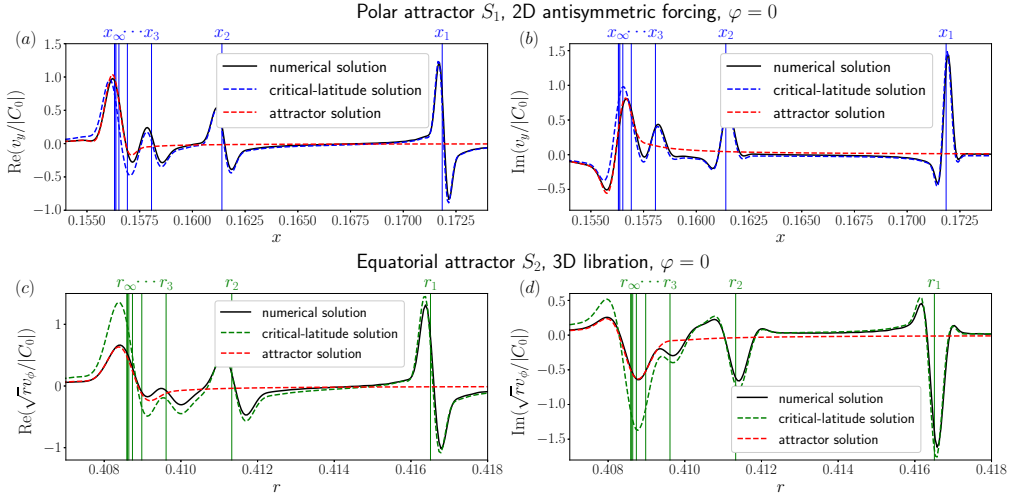


Figure 8: Comparison of velocity profiles between the numerical solution, the critical-latitude solution and the attractor solution at $E = 10^{-11}$: (ab) the cut S_1 of the polar attractor forced by the 2D antisymmetric forcing; (cd) the cut S_2 of the equatorial attractor forced the 3D libration (the other 2D forcings for the equatorial attractor show the same results as (cd)).

640 in that case which could explain why no significant attractor contribution was observed in
 641 the numerical solution when there is a phase shift. Finding the correct asymptotic form of
 642 the attractor solution in the presence of a phase shift is not an easy task. We leave it for future
 643 studies, probably in a simpler geometry.

644

4.2. Results

645 We now try to assess the performance of the attractor solution discussed above and see
 646 whether the rather poor performance of the critical-latitude solution (3.27) for the cases
 647 without phase shift (the polar attractor forced by the 2D antisymmetric forcing in figure
 648 5(e*f*) and the equatorial attractors in figure 6) is improved. Since all the three forcings are
 649 imposed on the inner core, only one vertex for each attractor is forced, namely $P_{0,\infty}^{(P)}$ for the
 650 polar attractor and $P_{0,\infty}^{(E)}$ for the equatorial attractor (see figure 4b). The forcing term δ (4.4,
 651 4.15) can be simplified to

$$652 \quad \delta = \begin{cases} \psi_{0,\infty}^{(EP)}, & 2D; \\ \psi_{0,\infty}^{(EP)}/\sqrt{r_{0,\infty}}, & 3D. \end{cases} \quad (4.19)$$

653 The values of the Ekman pumping at the positions $P_{0,\infty}^{(P)}$ and $P_{0,\infty}^{(E)}$ correspond to the formulae
 654 of the inner core in table 2 of Appendix B. As shown in figure 8, the attractor solution (in red
 655 color) performs much better than the previous critical-latitude solution. It demonstrates the
 656 necessity of including the Ekman pumping into the asymptotic solution as one gets close to
 657 the attractor, especially for the attractors without phase shift. However, it is unnecessary for
 658 the attractors with phase shift as shown by 5(abcd), since there is no logarithmic singularity.

659 Note that we now face the problem of defining a transition between the critical-latitude
 660 solution valid during the first cycles and the attractor solution eventually valid close to the
 661 attractor. While we do not discuss this aspect of the problem in this paper, further studies
 662 would be required to clarify this transition.

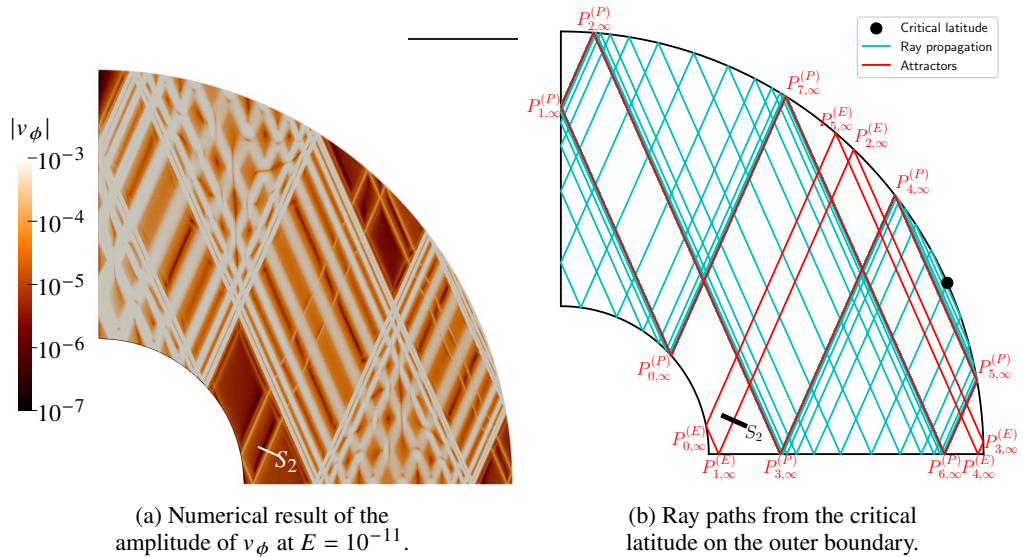


Figure 9: Results corresponding to the 3D libration of the outer boundary for $\eta = 0.35$ and $\omega = 0.8102$.

663 The forcings considered up to now were imposed on the inner core, which excites the wave
 664 beams from the critical latitude on the inner core. These wave beams propagate towards
 665 the attractors and coexist with them. In order to further validate the attractor solution, it is
 666 helpful to consider a configuration where the attractor is not affected by the propagation of
 667 the wave beams from the forced critical latitude. Fortunately, such configuration exists for
 668 the same aspect ratio and frequency but with the forcing imposed on the outer boundary. The
 669 wave pattern of the 3D libration on the outer boundary is shown in figure 9a, which can be
 670 compared to the ray paths in figure 9b. Since only the critical latitude on the outer boundary is
 671 forced, the only option for the initial propagation direction is pointing into the bulk. As shown
 672 in figure 9b, this ray (in cyan color) propagates onto the polar attractor. The corresponding
 673 wave beam from the critical latitude on the outer boundary should possess $E^{1/5}$ width and
 674 $E^{1/5}$ amplitude (Roberts & Stewartson 1963; Noir *et al.* 2001; Lin & Noir 2021), but it will
 675 not be our concern here. More importantly, figure 9a shows that the equatorial attractor is
 676 still present although it is not connected to the ray emerging from the critical latitude on the
 677 outer boundary. It should thus be directly forced by the Ekman pumping at the positions of
 678 the attractor on the outer boundary. The attractor solution can be built for this attractor since
 679 there is no phase shift associated with it. Because the vertices $P_{2,\infty}^{(E)}$, $P_{3,\infty}^{(E)}$ and $P_{5,\infty}^{(E)}$ of the
 680 equatorial attractor are forced, the forcing term δ (4.4, 4.15) can be simplified to

$$681 \quad \delta = \begin{cases} \psi_{2,\infty}^{(EP)} - \psi_{3,\infty}^{(EP)} - \psi_{5,\infty}^{(EP)}, & 2D; \\ \psi_{2,\infty}^{(EP)} / \sqrt{F_{2,\infty}} - \psi_{3,\infty}^{(EP)} / \sqrt{F_{3,\infty}} - \psi_{5,\infty}^{(EP)} / \sqrt{F_{5,\infty}}, & 3D. \end{cases} \quad (4.20)$$

682 The values of the Ekman pumping at the positions $P_{2,\infty}^{(E)}$, $P_{3,\infty}^{(E)}$ and $P_{5,\infty}^{(E)}$ correspond to the
 683 formulae of the outer boundary in table 2 of Appendix B. Figure 10 shows the comparison
 684 between the attractor solutions and the numerical solutions for the three forcings at three
 685 Ekman numbers. The amplitudes of the three forcings are rescaled. Good performance of the
 686 attractor solution is observed. As the Ekman number decreases, the agreement between the
 687 two solutions becomes better. The small ripples on the negative side of the similarity variable

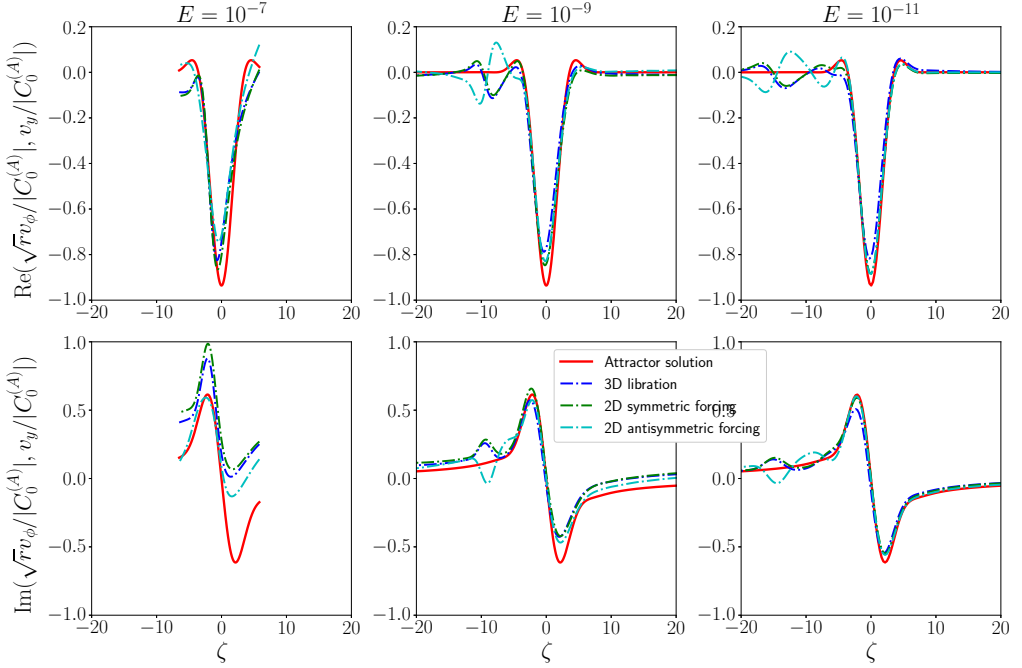


Figure 10: Comparison of velocity profiles between the attractor solutions and the numerical solutions on the cut S_2 of the equatorial attractor excited by the three forcings imposed on the outer boundary at three Ekman numbers.

688 at the low Ekman numbers are wave beams from the critical latitude on the unforced inner
 689 core. They are much weaker and the accumulation of them on the attractor remain negligible
 690 compared to the attractor beam. Figure 11 shows the Ekman number scalings of the attractor
 691 beams with a beam width and a velocity amplitude in $E^{1/3}$ and $E^{1/6}$ respectively, as expected.

692 To summarise, we have seen that the solution close to an attractor without phase shift is well-
 693 described by our asymptotic solution obtained by keeping only the logarithmic singularity
 694 contribution of the inviscid expression of the streamfunction. This has been observed for all
 695 types of forcing, in 2D and in 3D, and for configurations where the attractor is connected to
 696 the critical latitude or not.

697 5. Conclusion

698 Using asymptotic analysis and numerical integration, we have studied the linear harmonic
 699 solution obtained in a rotating spherical shell by librating the inner or outer boundary for
 700 very small Ekman numbers. We have considered a shell aspect ratio and a forcing frequency
 701 such that the ray beams converge towards either a polar attractor touching the rotation axis,
 702 or an equatorial attractor not touching the rotation axis. Both 3D axisymmetric and 2D
 703 configurations with different types of forcing have been considered to analyse the effect of
 704 the geometric singularity on the axis (obtained in 3D) and the influence of a phase shift
 705 (present in the polar attractor in 3D and in 2D with a symmetric forcing).

706 We have focused our interest on the concentrated internal shear layers that appear along
 707 the ray emitted from the critical latitude on the inner core, and close to the attractors.

708 We have first shown, that, when the forcing is performed on the inner core, the dominant
 709 part of the solution is associated with a critical latitude beam. We have shown that the

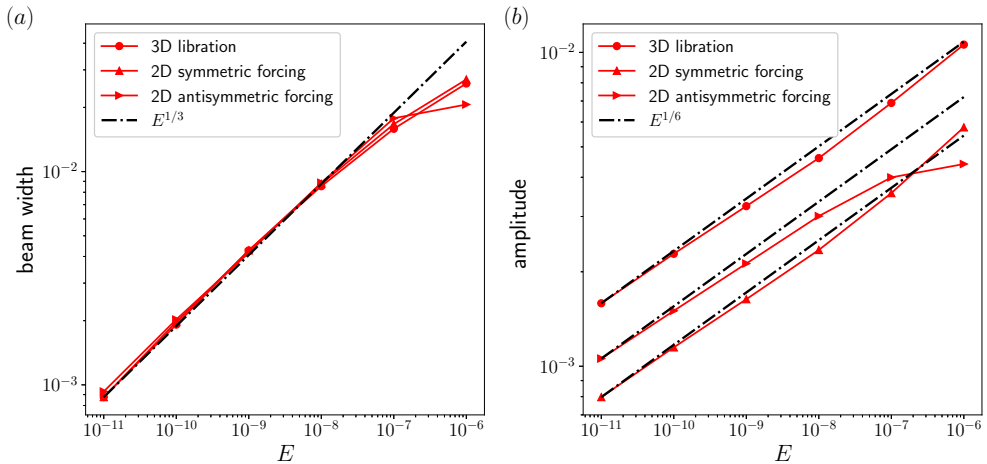


Figure 11: Ekman number scalings of the equatorial attractor excited by the three forcings imposed on the outer boundary: (a) beam width measured by the distance of the peaks of the profiles in figure 10; (b) velocity amplitude taken at the critical position.

710 characteristics of this beam are obtained by propagating the self-similar solution issued from
 711 the critical latitude on the inner core, as in an unbounded geometry (Le Dizès & Le Bars
 712 2017) or for periodic ray paths (HFRL22). This self-similar solution has a width in $E^{1/3}$,
 713 a well-defined velocity amplitude in $E^{1/12}$, and a velocity structure corresponding to the
 714 singularity index $m = 5/4$. As it propagates and reflects on boundaries (and possibly on the
 715 axis), its amplitude decreases down to $E^{1/6}$ until it reaches one of the two attractors.

716 We have then observed that the numerical solution departs from the asymptotic critical-
 717 latitude solution when we get close to the attractor, for some of the attractors. We have seen
 718 that the departure was present when the rays do not exhibit a phase shift along the attractor,
 719 that is for the equatorial attractor and for the polar attractor in 2D with an antisymmetric
 720 forcing. We have then constructed a new asymptotic solution to describe the solution close
 721 to such an attractor, using results from O05. The main idea is based on the derivation of
 722 an inviscid functional equation for the streamfunction obtained by propagating the solution
 723 on a complete cycle on the attractor taking into account contraction/expansion as well as
 724 Ekman pumping from the boundaries. The equation that is obtained when there is no phase
 725 shift is the equation obtained by O05. We have solved this equation by keeping only the
 726 logarithmic singular part. When smoothed by viscosity, this singular behavior leads to a
 727 self-similar expression for the velocity with a singularity index $m = 1$ and an amplitude
 728 in $E^{1/6}$. Contrarily to the critical-latitude solution, the amplitude of this attractor solution
 729 depends on the Ekman pumping at the locations where the attractor touches the boundaries.
 730 We have shown that it describes correctly the numerical solution close to the attractor for all
 731 the attractors without phase shift.

732 From an asymptotic point of view, it would now be useful to obtain a solution which
 733 describes both the critical solution and the attractor solution in order to understand how the
 734 index characterising the self-similar solution changes from $m = 5/4$ to $m = 1$.

735 When the attractor exhibits a phase shift, the analysis of O05 cannot be completely applied.
 736 We have seen that a different functional equation is obtained for the streamfunction which
 737 does not possess any logarithmically singular solution. We suspect that the amplitude of the
 738 solution is weaker in that case which could explain why its contribution is not visible in the

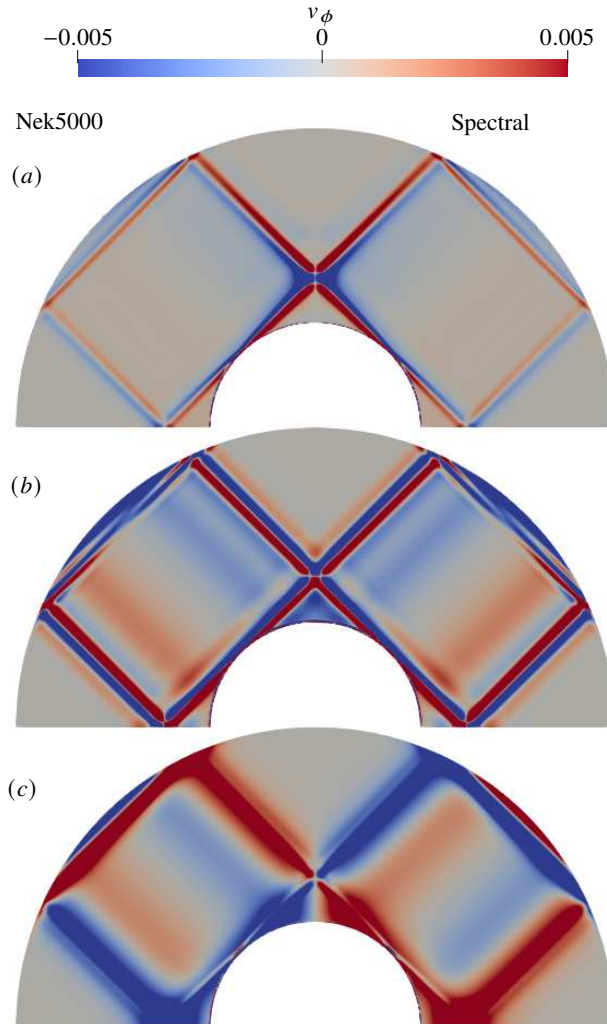


Figure 12: Comparison between the direct numerical results given by Nek5000 and the spectral codes: (a) 3D libration; (b) 2D symmetric forcing; (c) 2D antisymmetric forcing. The combination of the aspect ratio and forcing frequency is $(\eta, \omega) = (0.35, \sqrt{2})$.

739 numerical solution close to the attractor. Obtaining an asymptotic expression describing the
 740 solution in that case still constitutes one of the important remaining issues.

741 **Acknowledgements.** J. He acknowledges China Scholarship Council for financial support (CSC
 742 202008440260). Centre de Calcul Intensif d'Aix-Marseille is acknowledged for granting access to its
 743 high performance computing resources.

744 **Declaration of interests.** The authors report no conflict of interest.

745 Appendix A. Verification of the spectral codes

746 The spectral codes are verified against the open-source spectral-element software NEK5000
 747 (Fischer 1997) (NEK5000 Version 19.0, Argonne National Laboratory, Illinois; available
 748 at <https://nek5000.mcs.anl.gov>). This code has already been used in the context of inertial

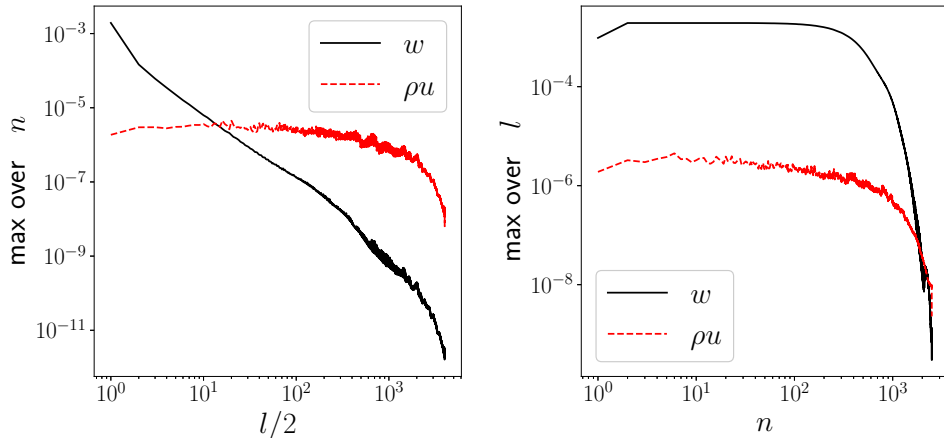


Figure 13: Spectra of the spherical harmonic components (a) and the Chebyshev coefficients (b) at $E = 10^{-11}$ with the resolution $(N, L) = (2500, 8000)$. For each l or n , the maximum value over the other spectral component is taken. The forcing corresponds to the 3D libration imposed on the inner core. The aspect ratio is $\eta = 0.35$ and the forcing frequency is $\omega = 0.8102$.

749 wave propagation (Favier *et al.* 2014). Linear temporal simulations with the time-harmonic
 750 forcing are implemented by NEK5000. After enough number of periods, the time-harmonic
 751 steady state is reached and the results at different instants are extracted to compare with the
 752 real and the imaginary parts of the spectral results. Since it is almost impossible to reach
 753 the very low Ekman number 10^{-11} when solving the initial value problem with Nek5000,
 754 the comparison is done at the relative high Ekman number 10^{-6} . The simulations are run
 755 for all three forcings considered in this work. In the 3D configuration, the simulation is run
 756 in the upper-right quarter of an annulus, with the axisymmetric and symmetric boundary
 757 conditions set on the two straight boundaries respectively. In the 2D configuration, the
 758 simulations are run in the upper half of an annulus, with symmetric boundary conditions
 759 set on the two straight boundaries. One of the curved boundaries is subject to the harmonic
 760 forcing, while the other is subject to the no-slip boundary condition. The aspect ratio and
 761 the forcing frequency are chosen to be 0.35 and $\sqrt{2}$ respectively, so that the wave pattern is
 762 a simple periodic orbit as in HFRL22. The comparisons are shown in figure 12. The results
 763 of NEK5000 are shown on the left side, while those of the spectral codes are shown on the
 764 right side. They agree with each other very well.

765 On the other hand, the convergence of the spectral codes is verified by the spectra of
 766 the spherical harmonic (or Fourier) components and the Chebyshev coefficients, as in
 767 Rieutord & Valdettaro (1997). Figure 13 shows the spectra for the 3D libration imposed
 768 on the inner core with the aspect ratio 0.35 and forcing frequency 0.8102 at the lowest
 769 Ekman number 10^{-11} . The 2D results are similar and omitted.

770 Appendix B. Ekman pumping

771 The viscous forcing generates an Ekman layer adjacent to the boundary. The Ekman pumping
 772 plays a role in the generation of wave beams in the bulk. In order to derive the formula of it,
 773 it is convenient to use the streamfunction expression in the spherical or polar coordinates.

B.1. 3D configuration

774

775 We first consider the libration imposed on the inner core. In the spherical coordinates (ρ, θ, ϕ) ,
776 the streamfunction ψ and the associated variable χ are defined as

$$777 \quad v_\rho = \frac{1}{\rho^2 \sin \theta} \frac{\partial \psi}{\partial \theta}, \quad v_\theta = -\frac{1}{\rho \sin \theta} \frac{\partial \psi}{\partial \rho}, \quad v_\phi = \frac{\chi}{\rho \sin \theta}. \quad (\text{B } 1)$$

The governing equations (2.3) are recast to

$$-i\omega D^2 \psi + 2(\cos \theta \frac{\partial \chi}{\partial \rho} - \frac{\sin \theta}{\rho} \frac{\partial \chi}{\partial \theta}) - ED^4 \psi = 0, \quad (\text{B } 2a)$$

$$-i\omega \chi - 2(\cos \theta \frac{\partial \psi}{\partial \rho} - \frac{\sin \theta}{\rho} \frac{\partial \psi}{\partial \theta}) - ED^2 \chi = 0, \quad (\text{B } 2b)$$

778 with the operator

$$779 \quad D^2 = \frac{\partial^2}{\partial \rho^2} - \frac{1}{\rho^2 \tan \theta} \frac{\partial}{\partial \theta} + \frac{1}{\rho^2} \frac{\partial^2}{\partial \theta^2}, \quad (\text{B } 3)$$

and the boundary conditions

$$\psi = \partial \psi / \partial \rho = 0, \quad \chi = \eta^2 \sin^2 \theta \quad \text{at} \quad \rho = \eta, \quad (\text{B } 4a)$$

$$\psi = \partial \psi / \partial \rho = \chi = 0 \quad \text{at} \quad \rho = 1. \quad (\text{B } 4b)$$

780 The length scale of the Ekman layer is \sqrt{E} . The radial distance to the centre is rescaled as

$$781 \quad \hat{\rho} = (\rho - \eta) / \sqrt{E}. \quad (\text{B } 5)$$

782 The streamfunction ψ and the associated χ are expanded as to the leading order

$$783 \quad \psi = \sqrt{E} \hat{\psi}^{(1)}(\hat{\rho}, \theta), \quad \chi = \hat{\chi}^{(0)}(\hat{\rho}, \theta). \quad (\text{B } 6)$$

In the leading order, the governing equations (B 2) become

$$-i\omega \frac{\partial^2 \hat{\psi}^{(1)}}{\partial \hat{\rho}^2} + 2 \cos \theta \frac{\partial \hat{\chi}^{(0)}}{\partial \hat{\rho}} - \frac{\partial^4 \hat{\psi}^{(1)}}{\partial \hat{\rho}^4} = 0, \quad (\text{B } 7a)$$

$$-i\omega \hat{\chi}^{(0)} - 2 \cos \theta \frac{\partial \hat{\psi}^{(1)}}{\partial \hat{\rho}} - \frac{\partial^2 \hat{\chi}^{(0)}}{\partial \hat{\rho}^2} = 0, \quad (\text{B } 7b)$$

with the boundary conditions

$$\psi = \partial \psi / \partial \rho = 0, \quad \chi = \eta^2 \sin^2 \theta, \quad \text{as} \quad \hat{\rho} = 0, \quad (\text{B } 8a)$$

$$\partial \psi / \partial \rho \rightarrow 0, \quad \chi \rightarrow 0, \quad \text{as} \quad \hat{\rho} \rightarrow \infty. \quad (\text{B } 8b)$$

784 The solution of the streamfunction is obtained as

$$785 \quad \psi = \sqrt{E} i \frac{\eta^2 \sin^2 \theta}{2} \left(-\frac{e^{-\lambda_+ \hat{\rho}}}{\lambda_+} + \frac{1}{\lambda_+} + \frac{e^{-\lambda_- \hat{\rho}}}{\lambda_-} - \frac{1}{\lambda_-} \right), \quad (\text{B } 9)$$

786 with λ_\pm defined as

$$787 \quad \lambda_+ = (1 - i) \sqrt{\omega/2 + \cos \theta} \quad (\text{B } 10)$$

788 and

$$789 \quad \lambda_- = \begin{cases} (1 - i) \sqrt{\omega/2 - \cos \theta}, & \omega/2 > \cos \theta, \\ (1 + i) \sqrt{\cos \theta - \omega/2}, & \omega/2 < \cos \theta. \end{cases} \quad (\text{B } 11)$$

	3D libration	2D symmetric forcing	2D antisymmetric forcing
inner core	$i\eta^2 \sin^2 \theta/2$	$i/2$	$i\eta \sin \theta/2$
outer boundary	$-i \sin^2 \theta/2$	$-i/2$	$-i \sin \theta/2$

Table 2: Expressions of Ekman pumping $\psi^{(EP)}$ (divided by $\left(\frac{1}{\lambda_+} - \frac{1}{\lambda_-}\right)\sqrt{E}$) generated by different forcings.

790 When $\hat{\rho}$ goes to $+\infty$, the Ekman pumping is obtained as

$$791 \quad \psi^{(EP)} = \frac{i\eta^2 \sin^2 \theta}{2} \left(\frac{1}{\lambda_+} - \frac{1}{\lambda_-} \right) \sqrt{E}. \quad (\text{B } 12)$$

792 The Ekman pumping blows up at the critical co-latitude $\theta_c = \arccos \omega/2$.

793 When the libration is imposed on the outer boundary, the boundary conditions become
794 different and the corresponding Ekman pumping can be obtained similarly, which is

$$795 \quad \psi^{(EP)} = \frac{-i \sin^2 \theta}{2} \left(\frac{1}{\lambda_+} - \frac{1}{\lambda_-} \right) \sqrt{E}. \quad (\text{B } 13)$$

796 B.2. 2D configuration

797 In the 2D configuration, the governing equations (2.22) of the streamfunction and the
798 associated variable χ in the polar coordinates are solved asymptotically using the same
799 scaling $E^{1/2}$ as in the 3D configuration. The expressions of the Ekman pumping generated by
800 different forcings are given in table 2. Note that ϑ in the 2D configuration has been replaced
801 by $\pi/2 - \theta$ in order to keep the similar expressions as in the 3D counterpart.

802 Note that, the Ekman pumping is $O(E^{1/2})$, except at the critical latitude where the Ekman
803 pumping blows up.

REFERENCES

- 804 BEZANSON, J., EDELMAN, A., KARPINSKI, S. & SHAH, V. B. 2017 Julia: A fresh approach to numerical
805 computing. *SIAM Rev.* **59** (1), 65–98.
- 806 ENGELN-MÉULLGES, G. & UHLIG, F. 1996 *Numerical algorithms with C*. Springer Science & Business
807 Media.
- 808 FAVIER, B., BARKER, A. J., BARUTEAU, C. & OGIIVIE, G. I. 2014 Non-linear evolution of tidally forced
809 inertial waves in rotating fluid bodies. *Mon. Not. R. Astron. Soc.* **439** (1), 845–860.
- 810 FISCHER, P. F. 1997 An overlapping schwarz method for spectral element solution of the incompressible
811 navier–stokes equations. *J. Comput. Phys.* **133** (1), 84–101.
- 812 FLYNN, M. R., ONU, K. & SUTHERLAND, B. R. 2003 Internal wave excitation by a vertically oscillating
813 sphere. *J. Fluid Mech.* **494**, 65–93.
- 814 GHAEMSAIDI, S. J. & PEACOCK, T. 2013 3D Stereoscopic PIV visualization of the axisymmetric conical
815 internal wave field generated by an oscillating sphere. *Exp. Fluids* **54** (2), 1454.
- 816 GREENSPAN, H. P. 1968 *The theory of rotating fluids*. CUP Archive.
- 817 HE, J., FAVIER, B., RIEUTORD, M. & LE DIZÈS, S. 2022 Internal shear layers in librating spherical shells: The
818 case of periodic characteristic paths. *J. Fluid Mech.* **939**.
- 819 HURLEY, D. G. 1997 The generation of internal waves by vibrating elliptic cylinders. Part 1. Inviscid solution.
820 *J. Fluid Mech.* **351**, 105–118.
- 821 HURLEY, D. G. & KEADY, G. 1997 The generation of internal waves by vibrating elliptic cylinders. Part 2.
822 Approximate viscous solution. *J. Fluid Mech.* **351**, 119–138.
- 823 JOUVE, L. & OGIIVIE, G. I. 2014 Direct numerical simulations of an inertial wave attractor in linear and
824 nonlinear regimes. *J. Fluid Mech.* **745**, 223–250.

- 825 KERSWELL, R. R. 1995 On the internal shear layers spawned by the critical regions in oscillatory Ekman
826 boundary layers. *J. Fluid Mech.* **298**, 311–325.
- 827 KIDA, S. 2011 Steady flow in a rapidly rotating sphere with weak precession. *J. Fluid Mech.* **680**, 150–193.
- 828 LE DIZÈS, S. 2020 Reflection of oscillating internal shear layers: Nonlinear corrections. *J. Fluid Mech.* **899**,
829 A21.
- 830 LE DIZÈS, S. 2023 Critical slope singularities in rotating and stratified fluids (hal-04167978).
- 831 LE DIZÈS, S. & LE BARS, M. 2017 Internal shear layers from librating objects. *J. Fluid Mech.* **826**, 653–675.
- 832 LIN, Y. & NOIR, J. 2021 Libration-driven inertial waves and mean zonal flows in spherical shells. *Geophys.*
833 *Astrophys. Fluid Dyn.* **115** (3), 258–279.
- 834 MAAS, L., BENIELLI, D., SOMMERIA, J. & LAM, F.-P. 1997 Observation of an internal wave attractor in a
835 confined, stably stratified fluid. *Nature* **388** (6642), 557–561.
- 836 MAAS, L. R. M. & LAM, F. A. 1995 Geometric focusing of internal waves. *J. Fluid Mech.* **300**, 1–41.
- 837 MACHICOANE, N., CORTET, P., VOISIN, B. & MOISY, F. 2015 Influence of the multipole order of the source
838 on the decay of an inertial wave beam in a rotating fluid. *Phys. Fluids* **27** (6), 066602.
- 839 MOORE, D. W. & SAFFMAN, P. G. 1969 The structure of free vertical shear layers in a rotating fluid and the
840 motion produced by a slowly rising body. *Philos. Trans. R. Soc. London, Ser. A* **264** (1156), 597–634.
- 841 NOIR, J., JAULT, D. & CARDIN, P. 2001 Numerical study of the motions within a slowly precessing sphere at
842 low Ekman number. *J. Fluid Mech.* **437**, 283–299.
- 843 OGILVIE, G. I. 2005 Wave attractors and the asymptotic dissipation rate of tidal disturbances. *J. Fluid Mech.*
844 **543**, 19–44.
- 845 OGILVIE, G. I. 2009 Tidal dissipation in rotating fluid bodies: A simplified model. *Mon. Not. R. Astron. Soc.*
846 **396** (2), 794–806.
- 847 OGILVIE, G. I. 2020 Internal waves and tides in stars and giant planets. In *Fluid Mechanics of Planets and*
848 *Stars*, pp. 1–30. Springer.
- 849 OGILVIE, G. I. & LIN, D. N. C. 2004 Tidal Dissipation in Rotating Giant Planets. *ApJ* **610** (1), 477–509.
- 850 RABITTI, A. & MAAS, L. R. M. 2013 Meridional trapping and zonal propagation of inertial waves in a
851 rotating fluid shell. *J. Fluid Mech.* **729**, 445–470.
- 852 RIEUTORD, M. 1991 Linear theory of rotating fluids using spherical harmonics. II. Time periodic flows.
853 *Geophys. Astrophys. Fluid Dyn.* **59**, 185–208.
- 854 RIEUTORD, M., GEORGEOT, B. & VALDETTARO, L. 2000 Wave Attractors in Rotating Fluids: A Paradigm for
855 Ill-Posed Cauchy Problems. *Phys. Rev. Lett.* **85** (20), 4277–4280.
- 856 RIEUTORD, M., GEORGEOT, B. & VALDETTARO, L. 2001 Inertial waves in a rotating spherical shell: Attractors
857 and asymptotic spectrum. *J. Fluid Mech.* **435**, 103–144.
- 858 RIEUTORD, M. & VALDETTARO, L. 1997 Inertial waves in a rotating spherical shell. *J. Fluid Mech.* **341**,
859 77–99.
- 860 RIEUTORD, M. & VALDETTARO, L. 2010 Viscous dissipation by tidally forced inertial modes in a rotating
861 spherical shell. *J. Fluid Mech.* **643**, 363–394.
- 862 RIEUTORD, M., VALDETTARO, L. & GEORGEOT, B. 2002 Analysis of singular inertial modes in a spherical
863 shell: The slender toroidal shell model. *J. Fluid Mech.* **463**, 345–360.
- 864 ROBERTS, P. H. & STEWARTSON, K. 1963 On the stability of a MacLaurin spheroid of small viscosity.
865 *Astrophys. J.* **137** (3), 777–790.
- 866 SUTHERLAND, B. R. & LINDEN, P. F. 2002 Internal wave excitation by a vertically oscillating elliptical
867 cylinder. *Phys. Fluids* **14** (2), 721–731.
- 868 THOMAS, N. H. & STEVENSON, T. N. 1972 A similarity solution for viscous internal waves. *J. Fluid Mech.*
869 **54** (3), 495–506.
- 870 TILGNER, A. 1999 Driven inertial oscillations in spherical shells. *Phys. Rev. E* **59**, 1789–1794.
- 871 VOISIN, B. 2003 Limit states of internal wave beams. *J. Fluid Mech.* **496**, 243–293.
- 872 VOISIN, B., ERMANYUK, E. V. & FLÓR, J.-B. 2011 Internal wave generation by oscillation of a sphere, with
873 application to internal tides. *J. Fluid Mech.* **666**, 308–357.
- 874 ZHANG, H. P., KING, B. & SWINNEY, HARRY L. 2007 Experimental study of internal gravity waves generated
875 by supercritical topography. *Phys. Fluids* **19** (9), 096602.